


# Integrated Sensing and Communications for End-to-End Predictive Beamforming Design in Vehicle-to-Infrastructure Networks

Zihuan Wang , *Student Member, IEEE*, Vincent W.S. Wong , *Fellow, IEEE*, and Robert Schober , *Fellow, IEEE*

**Abstract**—Integrated sensing and communications (ISAC) has emerged as a promising technology for predictive beamforming in vehicle-to-infrastructure (V2I) networks. Most of the existing works on ISAC assume each vehicle is equipped with a single antenna and use a two-phase scheme for predictive beamforming design. In the first phase, the reflected sensing signals at the roadside unit (RSU) are used to estimate the state parameters (e.g., angle, channel state information (CSI)) of the vehicles. In the second phase, the beamformer is predicted based on the estimated state parameters. The two-phase scheme suffers from the drawback that the estimation error in the first phase can impact the beamformer design in the second phase and may lead to a degradation in the achievable rate. In this work, we design predictive beamformers for both the RSU and vehicles in an end-to-end manner by using deep learning. We propose one-sided predictive beamforming (OSPB) and two-sided predictive beamforming (TSPB) schemes, where the beamformers for the vehicles are determined by the RSU and by the vehicles themselves, respectively. Both schemes directly predict the beamformers based on the reflected sensing signals via deep neural networks (DNNs). Compared with the existing two-phase schemes, the proposed schemes bypass the intermediate parameter estimation phase, thereby mitigating the impact of parameter estimation error. Our simulation results demonstrate the advantages of the proposed schemes over the two-phase baseline schemes in terms of achievable sum-rate.

**Index Terms**—Deep learning, end-to-end design, integrated sensing and communications (ISAC), predictive beamforming, vehicle-to-infrastructure (V2I) networks.

Received 25 June 2023; revised 11 February 2024 and 5 July 2024; accepted 23 September 2024. Date of publication 3 October 2024; date of current version 8 January 2025. The work of Zihuan Wang and Vincent W.S. Wong was supported in part by the Government of Canada Innovation for Defence Excellence and Security (IDEaS) Program and in part by the Digital Research Alliance of Canada (alliancecan.ca). The work of Robert Schober was supported in part by the Federal Ministry of Education and Research of Germany through the Programme of “Souverän. Digital. Vernetzt.” joint Project 6G-RIC under Project PIN 16KISK023 and in part by Deutsche Forschungsgemeinschaft (DFG, German Research Foundation) under Grant SCHO 831/15-1. An earlier version of this paper was published at the Proceedings of IEEE International Conference on Communications (ICC), May 2023 [DOI: 10.1109/ICC45041.2023.10279351]. The guest editor coordinating the review of this article and approving it for publication was Dr. Nuria Gonzalez-Prelcic. (*Corresponding author: Vincent W.S. Wong.*)

Zihuan Wang and Vincent W.S. Wong are with the Department of Electrical and Computer Engineering, The University of British Columbia, Vancouver, BC V6T 1Z4, Canada (e-mail: zihuanwang@ece.ubc.ca; vincentw@ece.ubc.ca).

Robert Schober is with the Institute for Digital Communications, Friedrich-Alexander University of Erlangen-Nuremberg, 91058 Erlangen, Germany (e-mail: schober@lnt.de).

Digital Object Identifier 10.1109/JSTSP.2024.3474254

## I. INTRODUCTION

### A. Background

THE sixth-generation (6G) wireless networks are expected to support various emerging applications and use cases. Applications such as autonomous and connected vehicles require both wireless connectivity and sensing capability [2], [3], [4], [5]. Traditionally, sensing and communication systems have used separate spectrum resources and are operated independently. Today, the use of higher frequency bands and larger antenna arrays facilitates the wireless communication networks to perform sensing. With the development of millimeter-wave (mmWave) and massive multiple-input multiple-output (MIMO) technologies, future 6G wireless networks are expected to become perceptive, where the base stations and roadside units (RSUs) can not only provide communications functionality but also obtain situational information through sensing. This has stimulated the development of integrated sensing and communications (ISAC) techniques [6], [7]. ISAC integrates the sensing and communications functionalities into a single system. It enables these two modules to share the same hardware and spectrum. The coexistence of sensing and communications can reduce hardware cost, facilitate the creation of new services, and improve spectral and energy efficiencies.

ISAC systems can provide communications and target sensing functionalities simultaneously through beamforming [8], [9], [10], [11]. One of the key applications of ISAC is predictive beamforming for vehicle-to-infrastructure (V2I) networks [12], [13], [14], [15]. By deploying a large-scale antenna array at the RSU, V2I networks can provide enhanced mobile broadband (eMBB) services to vehicles. To maintain a reliable communication session, it is crucial to direct the beamformer at the RSU toward the vehicles during data transmission. Conventionally, before data transmission begins, the RSU periodically transmits pilot signals using different beamformers [12]. Based on the received pilot signals, each vehicle determines the beamformer that leads to the highest received power and sends its index back to the RSU. The RSU then uses this beamformer for data transmission. However, the conventional scheme incurs high signaling overhead due to the frequent transmission of pilots and the corresponding uplink feedback signaling between the vehicles and the RSU. By using ISAC, the RSU can simultaneously send downlink signals to the vehicles and receive echo signals reflected by the bodies of the vehicles for sensing.

The RSU is then able to extract the temporal correlation of the received echo signals and predict the beamformer for future data transmissions. Compared with the conventional pilot-based schemes, ISAC-enabled predictive beamforming can reduce the overhead incurred by the pilot signals and the uplink feedback.

### B. Related Work

ISAC can be applied to a wide range of wireless communications systems which require sensing functionality, such as point-to-point mmWave systems [16], wireless mobile networks [17], distributed systems [18], intelligent reflecting surface assisted systems [19], vehicle-to-everything networks [20], vehicle-to-device networks [21], and vehicle-to-vehicle networks [22], [23]. In particular, ISAC techniques play a key role in predictive beamforming design for V2I networks, where sensing is leveraged to facilitate beamformer prediction. In [24], the position of a vehicle is first predicted based on the reflected sensing signals. Then, the beamformer is determined given the predicted position information. In [25], ISAC-enabled predictive beamforming for orthogonal time frequency space (OTFS) transmission in V2I networks is investigated. The Doppler shift and delay are predicted by exploiting the slow time-variations in the delay-Doppler domain. Subsequently, the beamformers are predicted using the estimated parameters.

The aforementioned works on predictive beamforming assume each vehicle is equipped with a single antenna. To enhance the data rate and reliability as well as to increase the degrees of freedom (DoF), each vehicle can be equipped with multiple antennas combined with receive beamforming [12], [13]. In [12], an extended Kalman filtering (EKF) scheme is proposed to estimate and track the angles of vehicles using the reflected sensing signals at the RSU. The transmit and receive beamformers are determined by the RSU based on the estimated angles. Then, the RSU forwards the predicted receive beamformers to the vehicles during downlink transmission. In [13], a factor graph based message passing algorithm is proposed for the angular parameter estimation. The transmit and receive beamformers are then predicted by the RSU. Moreover, deep learning based algorithms have shown great potential for predictive beamforming design. In [14], a deep learning based algorithm is developed to extract the historical angular parameters of the vehicles. Then, the beamformer is designed to align with the angle for maximization of the achievable rate. In [15], the channel state information (CSI) is first estimated by the RSU based on the angle and distance information. Then, the transmit beamformer is predicted using deep learning techniques. In particular, the developed historical channel-based convolutional long short-term memory (LSTM) network (HCL-Net) takes the estimated historical CSI as input and predicts the beamformer.

### C. Motivation and Contributions

Most of the existing works on ISAC-enabled predictive beamforming comprise two phases. In the first phase, given the reflected sensing signals, the state parameters (e.g., angle, CSI) of the channels of the vehicles are estimated. In the second phase, given the estimated parameters, the beamformers are

predicted with the objective to maximize the achievable sum-rate. However, the two-phase approach may suffer from performance degradation due to the estimation error introduced in the first phase. This will affect the subsequent beamforming design in the second phase and result in a degradation of the achievable sum-rate. To overcome this limitation, we propose an ISAC-enabled end-to-end predictive beamforming design that bypasses the intermediate parameter estimation phase. In our previous work [1], we developed such a scheme for V2I networks, where the RSU communicates with a single-antenna vehicle. Given the reflected sensing signals, the RSU directly predicts the transmit beamformer to maximize the achievable rate and maintain the communication link with the vehicle.

In this paper, we extend the system model in [1] to the multi-antenna multi-vehicle case, where each vehicle is equipped with an antenna array. We investigate the problem of transmit and receive beamformer prediction for the RSU and vehicles, respectively. In this work, the prediction of the transmit beamformer is implemented at the RSU since it has sufficient computational resources. For the receive beamformer of each vehicle, we consider the following two scenarios:

- *Scenario 1:* The vehicles do not have sufficient computational resources to determine the beamformer. Therefore, the receive beamformers for the vehicles are also predicted by the RSU.
- *Scenario 2:* The vehicles have sufficient computational resources. Each vehicle predicts its own receive beamformer locally.

To accommodate the aforementioned scenarios, we propose two different schemes, namely: ISAC-enabled one-sided predictive beamforming (OSPB) and two-sided predictive beamforming (TSPB). Both schemes predict the transmit and receive beamformers directly from the reflected sensing signals by using deep learning. The main contributions of this paper are summarized as follows:

- We first propose an OSPB scheme, where both the transmit and receive beamformers are predicted at the RSU. Given the reflected sensing signals, the RSU uses deep neural networks (DNNs) to determine the predictive transmit and receive beamformers in order to maximize the achievable sum-rate. The intermediate state parameter estimation phase typically required for the existing predictive beamforming schemes is bypassed. After prediction, the RSU informs the vehicles their receive beamformers during downlink transmission.
- We also propose a TSPB scheme, where the transmit and receive beamformers are determined using DNNs at the RSU and the vehicles, respectively. The proposed TSPB scheme allows each vehicle to predict its corresponding receive beamformer locally based on its previously employed receive beamformer. The TSPB scheme further eliminates the overhead of transmitting the predicted receive beamformers from the RSU to the vehicles.
- For the proposed OSPB and TSPB schemes, we develop DNNs which can directly map the reflected sensing signals to transmit and receive beamformers in an end-to-end manner. The developed DNNs extract the spatio-temporal

features of the reflected sensing signals through a convolutional neural network (CNN), an LSTM network, and an attention module.

- We conduct simulations to evaluate the proposed OSPB and TSPB schemes. We compare our proposed schemes with seven baseline schemes, including three classic beamforming schemes (i.e., minimum mean square error (MMSE) beamforming, zero-forcing (ZF) beamforming, and singular value decomposition (SVD) based beamforming) with perfect CSI, as well as the EKF scheme in [12], an E-HCL beamforming scheme which is an extended version of the HCL-Net algorithm proposed in [15], and two deep learning neural network (i.e., fully-connected (FC) neural network and CNN) based beamforming schemes. Our numerical results demonstrate the benefits of the end-to-end design of the proposed schemes. The performance advantages become more significant as the number of vehicles increases, due to the joint design of the transmit and receive beamformers, providing better flexibility in managing inter-vehicle interference. Moreover, our results also demonstrate the robustness of the proposed schemes against noise in the reflected sensing signals.

#### D. Paper Structure and Notations

The rest of this paper is organized as follows. The system model for ISAC-enabled predictive beamforming in V2I networks is introduced in Section II. The proposed OSPB and TSPB schemes are presented in Sections III and IV, respectively. Performance evaluations and comparisons are provided in Section V. Finally, conclusions are drawn in Section VI.

**Notations:** We use boldface lower case letters and boldface upper case letters to denote vectors and matrices/tensors, respectively.  $(\cdot)^*$ ,  $(\cdot)^T$ , and  $(\cdot)^H$  are used to denote the conjugate, transpose, and conjugate transpose of a vector or matrix, respectively.  $\mathbb{C}^N$  and  $\mathbb{R}^N$  denote the sets of  $N$ -dimensional vectors with complex entries and real entries, respectively.  $\mathcal{CN}(\mu, \Sigma)$  denotes the complex Gaussian distribution, where  $\mu$  and  $\Sigma$  are the mean vector and covariance matrix, respectively.  $\mathbf{I}_N$  indicates an identity matrix of size  $N$ . We use  $j$  to denote the imaginary unit which satisfies  $j^2 = -1$ .  $\text{Re}(\cdot)$  and  $\text{Im}(\cdot)$  extract the real part and imaginary part of a complex number, respectively.  $\mathbb{E}\{\cdot\}$  denotes the expected value of a random variable. Finally,  $\otimes$  denotes the Kronecker product.

## II. SYSTEM MODEL

In this paper, we consider a V2I network with one RSU communicating with  $K$  vehicles in a road segment. We assume that two uniform planar arrays (UPAs) are equipped at the RSU for transmission and reception, respectively. Each vehicle has one UPA. The vehicles move along a single-lane road which is parallel to the transmit and receive UPAs of the RSU [12]. The transmit UPA of the RSU is equipped with  $N_t = N_h^{(\text{tx})} \times N_v^{(\text{tx})}$  antennas for downlink transmission, where  $N_h^{(\text{tx})}$  and  $N_v^{(\text{tx})}$  denote the number of antennas in horizontal and vertical dimension, respectively. Similarly, the receive UPA of the RSU

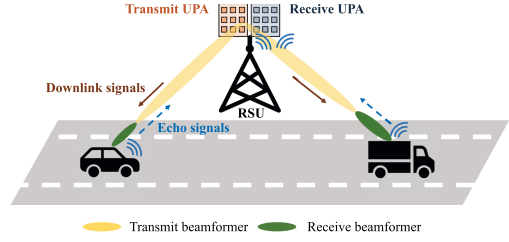


Fig. 1. System model of an RSU communicating with two vehicles in the considered V2I network.

is equipped with  $N_r = N_h^{(\text{rx})} \times N_v^{(\text{rx})}$  receive antennas, where  $N_h^{(\text{rx})}$  and  $N_v^{(\text{rx})}$  denote the number of horizontal and vertical antennas, respectively. The receive UPA is used for the reception of the reflected sensing signals. The UPA of each vehicle is parallel to the UPAs at the RSU, and has  $M_h$  horizontal antennas and  $M_v$  vertical antennas. The total number of antennas of the vehicle's UPA is given by  $M = M_h \times M_v$ . The RSU operates in the mmWave frequency band and communicates with the vehicles through line-of-sight (LoS) links. By leveraging full-duplex radio technology [26], the RSU equipped with ISAC functionality can receive the echo signals reflected from all vehicles for sensing purposes and perform downlink transmission simultaneously.<sup>1</sup> Fig. 1 illustrates a V2I network, where the RSU is communicating with two vehicles.

#### A. Sensing Model

We consider a time period  $T$ , during which the RSU maintains communication links with  $K$  vehicles. We divide the time period  $T$  into  $N$  time slots. The duration of each time slot is  $\Delta T$ . Let  $s_{k,n}(t)$  denote the transmitted signal to the  $k$ -th vehicle after transmit pulse shaping,<sup>2</sup>  $k = 1, \dots, K$ , at time instant  $t$  in time slot  $n \in \{1, \dots, N\}$ . The downlink signal for the  $K$  vehicles is given by  $\mathbf{s}_n(t) = [s_{1,n}(t) \cdots s_{K,n}(t)]^T \in \mathbb{C}^K$ . Similar to other recent works on predictive beamforming for V2I networks (e.g., [12], [13], [14], [15]), we assume that the state parameters (e.g., angle, CSI) of the channel of each vehicle remain constant during each time slot. Let  $\mathbf{F}_n = [\mathbf{f}_{1,n}, \dots, \mathbf{f}_{K,n}] \in \mathbb{C}^{N_t \times K}$  denote the transmit beamformer at the RSU in time slot  $n$ , where  $\mathbf{f}_{k,n}$  is the dedicated transmit beamformer for the  $k$ -th vehicle,  $k = 1, \dots, K$ . The beamformer remains the same within each time slot and changes between time slots. We further assume equal power allocation for the different vehicles' data streams [27], [28]. The transmitted signal  $\tilde{\mathbf{s}}_n(t) \in \mathbb{C}^{N_t}$  at time instant  $t$  in time slot  $n$  after beamforming can be expressed as

$$\tilde{\mathbf{s}}_n(t) = \mathbf{F}_n \mathbf{s}_n(t) = \sum_{k=1}^K \mathbf{f}_{k,n} s_{k,n}(t). \quad (1)$$

The transmitted signal  $\tilde{\mathbf{s}}_n(t)$  is partially reflected by the bodies of the vehicles. The reflected echo signals are received by the RSU.

<sup>1</sup> We assume the self-interference can be perfectly cancelled out.

<sup>2</sup> For simplicity of presentation, we assume a rectangular time-domain pulse shaping filter.



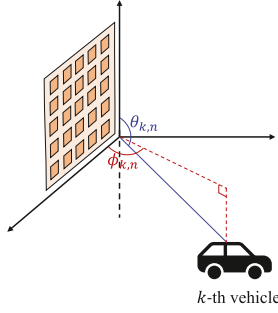


Fig. 2. The definition of the azimuth and elevation angles.

When UPAs are employed at the RSU and the vehicles, the transmitted and received signals are subject to beam steering. We use  $\mathbf{a}(\phi_{k,n}, \theta_{k,n}) \in \mathbb{C}^{N_t}$  to denote the transmit beam steering vector of the UPA at the RSU, where  $\phi_{k,n}$  and  $\theta_{k,n}$  are respectively the azimuth and elevation angles of departure (AoDs) from the RSU to the  $k$ -th vehicle in time slot  $n$ . We model the azimuth and elevation angles as in Fig. 2. For a half-wavelength-spaced UPA, the vertical and horizontal steering vectors can be expressed as follows [29]:

$$\mathbf{v}_v(\theta_{k,n}) = \frac{1}{\sqrt{N_v^{(tx)}}} \left[ 1 e^{-j\pi \cos \theta_{k,n}} \dots e^{-j(N_v^{(tx)}-1)\pi \cos \theta_{k,n}} \right]^T, \quad (2)$$

$$\mathbf{v}_h(\phi_{k,n}, \theta_{k,n}) = \frac{1}{\sqrt{N_h^{(tx)}}} \left[ 1 e^{-j\pi \sin \theta_{k,n} \cos \phi_{k,n}} \dots e^{-j(N_h^{(tx)}-1)\pi \sin \theta_{k,n} \cos \phi_{k,n}} \right]^T. \quad (3)$$

The beam steering vector  $\mathbf{a}(\phi_{k,n}, \theta_{k,n})$  is given by [29]

$$\mathbf{a}(\phi_{k,n}, \theta_{k,n}) = \mathbf{v}_h(\phi_{k,n}, \theta_{k,n}) \otimes \mathbf{v}_v(\theta_{k,n}). \quad (4)$$

Let  $\mathbf{b}(\phi_{k,n}, \theta_{k,n}) \in \mathbb{C}^{N_r}$  denote the beam steering vector of the receive UPA at the RSU.  $\mathbf{b}(\phi_{k,n}, \theta_{k,n})$  is also characterized by vertical and horizontal steering vectors, which are defined similarly as  $\mathbf{v}_v(\theta_{k,n})$  and  $\mathbf{v}_h(\phi_{k,n}, \theta_{k,n})$  in (2) and (3), respectively. The reflected echo signals received by the RSU at time instant  $t$  in time slot  $n$ ,  $\mathbf{r}_n(t) = [r_{1,n}(t) \dots r_{N_r,n}(t)]^T \in \mathbb{C}^{N_r}$ , are given by<sup>3</sup>

$$\mathbf{r}_n(t) = G \sum_{k=1}^K \beta_{k,n} e^{j2\pi\mu_{k,n}t} \mathbf{b}(\phi_{k,n}, \theta_{k,n}) \times \mathbf{a}^H(\phi_{k,n}, \theta_{k,n}) \tilde{\mathbf{s}}_n(t - \nu_{k,n}) + \mathbf{z}_n(t), \quad (5)$$

where  $G = \sqrt{N_t N_r}$  is the total antenna array gain.  $\nu_{k,n}$ ,  $\mu_{k,n}$ , and  $\beta_{k,n}$  are the time delay, Doppler frequency, and reflection

coefficient of the  $k$ -th vehicle in time slot  $n$ , respectively. According to [30], the reflection coefficient which includes the radar cross-section and path loss can be modeled as

$$\beta_{k,n} = \frac{\lambda \varrho_{k,n}}{(4\pi)^{3/2} d_{k,n}^{2\zeta}}, \quad (6)$$

where  $\lambda = f_c/c$  is the wavelength with  $f_c$  being the carrier frequency and  $c$  being the speed of the light.  $\varrho_{k,n}$  is the radar cross-section of the  $k$ -th vehicle in time slot  $n$  and  $d_{k,n}$  is the distance between the  $k$ -th vehicle and the RSU in time slot  $n$ .<sup>4</sup>  $\zeta$  is the path loss exponent.  $\mathbf{z}_n(t)$  is the complex white Gaussian noise.

Since the beam steering vectors of different vehicles are asymptotically orthogonal to each other [31, Section 2.5.3], i.e., for  $k \neq k'$ , we have  $|\mathbf{a}^H(\phi_{k,n}, \theta_{k,n}) \mathbf{a}(\phi_{k',n}, \theta_{k',n})| \approx 0$  and  $|\mathbf{b}^H(\phi_{k,n}, \theta_{k,n}) \mathbf{b}(\phi_{k',n}, \theta_{k',n})| \approx 0$ , the reflected echo signals received from different vehicles can be distinguished by the RSU and processed individually. For the  $k$ -th vehicle, the received echo signal at time instant  $t$  in time slot  $n$  is given by [12], [13]

$$\mathbf{r}_{k,n}(t) = G \beta_{k,n} e^{j2\pi\mu_{k,n}t} \mathbf{b}(\phi_{k,n}, \theta_{k,n}) \mathbf{a}^H(\phi_{k,n}, \theta_{k,n}) \mathbf{f}_{k,n} \times s_{k,n}(t - \nu_{k,n}) + \mathbf{z}_n(t). \quad (7)$$

Given the reflected echo signal of the  $k$ -th vehicle  $\mathbf{r}_{k,n}(t)$  at time instant  $t$  in time slot  $n$ , the time delay  $\nu_{k,n}$  and the Doppler frequency  $\mu_{k,n}$  can be estimated as follows [12], [13]:

$$\{\hat{\nu}_{k,n}, \hat{\mu}_{k,n}\} = \arg \max_{\nu, \mu} \left\| \int_0^{\Delta \tilde{T}_n} \mathbf{r}_{k,n}(t) s_{k,n}^*(t - \nu) e^{-j2\pi\mu t} dt \right\|^2, \quad (8)$$

where  $\hat{\nu}_{k,n}$  and  $\hat{\mu}_{k,n}$  are the estimated values.  $\Delta \tilde{T}_n$  is the time duration for data transmission in time slot  $n$ . We have  $\Delta \tilde{T}_n < \Delta T$ . After matched-filtering, delay-Doppler frequency compensation, and sampling, we obtain the reflected sensing signal  $\tilde{\mathbf{r}}_{k,n}$  of the  $k$ -th vehicle:<sup>5</sup>

$$\tilde{\mathbf{r}}_{k,n} = G \xi \beta_{k,n} \mathbf{b}(\phi_{k,n}, \theta_{k,n}) \mathbf{a}^H(\phi_{k,n}, \theta_{k,n}) \mathbf{f}_{k,n} + \bar{\mathbf{z}}_n, \quad (9)$$

where  $\xi$  is the matched-filtering gain. The value of  $\xi$  depends on the number of symbols transmitted during data transmission [12].  $\bar{\mathbf{z}}_n \sim \mathcal{CN}(\mathbf{0}, \sigma_r^2 \mathbf{I}_{N_r})$  is the measured noise in time slot  $n$  with zero mean and covariance matrix  $\sigma_r^2 \mathbf{I}_{N_r}$ .

## B. Communication Model

For communication, at time instant  $t$  in time slot  $n$ , all  $K$  vehicles receive downlink signals from the RSU. We use  $\mathbf{u}(\varphi_{k,n}, \vartheta_{k,n}) \in \mathbb{C}^M$  to denote the receive beam steering vector of the  $k$ -th vehicle in time slot  $n$ , where  $\varphi_{k,n}$  and  $\vartheta_{k,n}$

<sup>4</sup>Since the distance between the RSU and a vehicle is usually much larger than the antenna array size, each vehicle can be viewed as a single point target and the RSU can be viewed as a point source [12], [13], [14], [15].

<sup>5</sup>We note that delay and Doppler frequency compensation are typical signal processing techniques for sensing [32], and are different from state parameter (e.g., AoD, angle of arrival (AoA), CSI) estimation. In existing works, such as [12], [13], [14], [15], both delay and Doppler frequency compensation and state parameter estimation are required. In our work, the proposed schemes bypass the state parameter estimation phase.

<sup>3</sup>We assume that there is a dominant LoS link between the RSU and each vehicle [12], [13], [14], [15]. In practice, there may also exist clutter, which refers to the echoes reflected by objects other than the target of interest. We assume the contribution of the clutter to the received echo signals is small and incorporate the clutter interference into the noise term for simplicity. We investigate the impact of the clutter interference on the performance via simulations in Section V-E.

are the azimuth and elevation angles from the RSU to the  $k$ -th vehicle, respectively.  $\mathbf{u}(\varphi_{k,n}, \vartheta_{k,n})$  has the same structure as  $\mathbf{a}(\phi_{k,n}, \theta_{k,n})$ , cf. (2)–(4). Since the antenna array at each vehicle is parallel to the antenna arrays at the RSU, we have  $\varphi_{k,n} = \phi_{k,n}$  and  $\vartheta_{k,n} = \pi - \theta_{k,n}$ . Let  $\mathbf{w}_{k,n} \in \mathbb{C}^M$  denote the receive beamformer of the  $k$ -th vehicle in time slot  $n$ . Without loss of generality, we assume  $\|\mathbf{w}_{k,n}\|^2 = 1$ , for  $k = 1, \dots, K$ ,  $n = 1, \dots, N$ . We assume only the LoS link exists between the RSU and each vehicle.<sup>6</sup> Given the transmitted signal of the RSU from (1), the signal received by the  $k$ -th vehicle at time instant  $t$  in time slot  $n$  can be expressed as<sup>7</sup>

$$y_{k,n}(t) = \tilde{G} \sqrt{\alpha_{k,n}} e^{j \frac{2\pi}{\lambda} d_{k,n}} \mathbf{w}_{k,n}^H \mathbf{u}(\varphi_{k,n}, \vartheta_{k,n}) \mathbf{a}^H(\phi_{k,n}, \theta_{k,n}) \times \sum_{i=1}^K \mathbf{f}_{i,n} s_{i,n}(t) + \eta_{k,n}(t), \quad (10)$$

where  $\tilde{G} = \sqrt{N_t M}$  is the antenna gain.  $e^{j \frac{2\pi}{\lambda} d_{k,n}}$  denotes the phase of the LoS link.  $\eta_{k,n}(t)$  denotes the complex white Gaussian noise at the  $k$ -th vehicle in time slot  $n$ .  $\alpha_{k,n}$  is the path loss coefficient, which is defined as

$$\alpha_{k,n} = \alpha_0 \left( \frac{d_{k,n}}{d_0} \right)^{-\zeta}, \quad (11)$$

where  $\alpha_0$  is the path loss at reference distance  $d_0$ .

Assume the transmitted signal  $s_{k,n}(t)$ ,  $k = 1, \dots, K$ , from the RSU in time slot  $n$  has unit power. Then, after matched filtering and sampling, the received signal-to-noise ratio (SNR) at the  $k$ -th vehicle in time slot  $n$  can be expressed as

$$\gamma_{k,n}(\mathbf{f}_{k,n}, \mathbf{w}_{k,n}) = \frac{|\mathbf{w}_{k,n}^H \mathbf{H}_{k,n} \mathbf{f}_{k,n}|^2}{\sum_{i \neq k}^K |\mathbf{w}_{k,n}^H \mathbf{H}_{k,n} \mathbf{f}_{i,n}|^2 + \sigma_c^2}, \quad (12)$$

where  $\sigma_c^2$  is the variance of the sampled Gaussian noise and we define the communication channel matrix between the RSU and the  $k$ -th vehicle in time slot  $n$  as

$$\mathbf{H}_{k,n} = \tilde{G} \sqrt{\alpha_{k,n}} e^{j \frac{2\pi}{\lambda} d_{k,n}} \mathbf{u}(\varphi_{k,n}, \vartheta_{k,n}) \mathbf{a}^H(\phi_{k,n}, \theta_{k,n}). \quad (13)$$

Assuming the transmitted data symbols are independent and identically distributed Gaussian symbols, the achievable sum-rate of all the  $K$  vehicles in time slot  $n$  is given by

$$R_n = \sum_{k=1}^K \log_2 (1 + \gamma_{k,n}(\mathbf{f}_{k,n}, \mathbf{w}_{k,n})) = \sum_{k=1}^K \log_2 \left( 1 + \frac{|\mathbf{w}_{k,n}^H \mathbf{H}_{k,n} \mathbf{f}_{k,n}|^2}{\sum_{i \neq k}^K |\mathbf{w}_{k,n}^H \mathbf{H}_{k,n} \mathbf{f}_{i,n}|^2 + \sigma_c^2} \right). \quad (14)$$

<sup>6</sup>For mmWave frequencies, the channel is sparse and dominated by the LoS, as multipath components suffer much higher attenuation than the LoS link [33]. Here, for system design, we assume only LoS link exists. However, we evaluate the impact of the multipath components on the performance via simulations in Section V-E.

<sup>7</sup>In this work, we assume perfect time and frequency synchronization between the RSU and the vehicles. In the first time slot, synchronization can be achieved based on beam training during the initialization phase. In subsequent time slots, based on the estimated time delay and Doppler frequency  $\{\hat{\nu}_{k,n}, \hat{\mu}_{k,n}\}$ ,  $k = 1, \dots, K$ ,  $n > 1$ , obtained in (8), the RSU can then compensate the time and frequency offsets.

In time slot  $n$ , the objective is to determine the transmit and receive beamformers maximizing the achievable sum-rate. The corresponding problem can be formulated as follows:

$$\underset{\{\mathbf{f}_{k,n}, \mathbf{w}_{k,n}\}_{k=1}^K}{\text{maximize}} \quad \sum_{k=1}^K \log_2 (1 + \gamma_{k,n}(\mathbf{f}_{k,n}, \mathbf{w}_{k,n})) \quad (15a)$$

$$\text{subject to } \|\mathbf{f}_{k,n}\|^2 = \frac{P}{K}, \quad k = 1, \dots, K, \quad (15b)$$

where  $P$  denotes the maximum transmit power of the RSU. Constraint (15b) enforces that the same amount of power is allocated to all vehicles<sup>8</sup> [27], [28]. Note that the state parameters of a vehicle (e.g.,  $\theta_{k,n}$ ,  $\mathbf{H}_{k,n}$  for  $k = 1, \dots, K$ ) change from one time slot to another, which causes the optimal transmit and receive beamformers of the above problem also change over time. To maintain reliable downlink transmission in V2I networks, it is crucial for the RSU and each vehicle to direct the beamformers toward each other in each time slot. In conventional approaches, the RSU and vehicles obtain the transmit and receive beamformers based on frequent downlink pilot transmissions and uplink vehicles' feedback. However, this will inevitably incur communication latency and signaling overhead. By using ISAC, the transmit and receive beamformers can be predicted ahead of time, thus eliminating the need for additional pilot signals and feedback overhead. In particular, with the aid of ISAC, the time duration for data transmission can be simultaneously used for reflected sensing signal reception, such that the RSU can continuously collect the sensing information of the vehicles and extract the temporal correlation between consecutive data blocks for beamformer prediction.

Typically, the RSU predicts the transmit beamformer, as the RSU is able to gather the global sensing information of all vehicles and has sufficient computational resources. For the receive beamformer prediction for the vehicles, we consider two scenarios depending on where the receive beamformers are being computed: 1) at the RSU when vehicles have limited computational resources, and 2) locally at the vehicles. In the following sections, we propose two different schemes, namely the ISAC-enabled OSPB and TSPB schemes, for these two scenarios. We begin by presenting the proposed OSPB scheme in the next section.

### III. PROPOSED OSPB SCHEME

We assume that the RSU has established the initial communication links with the vehicles through conventional beam training, which requires pilot transmission and uplink feedback [12]. This allows the RSU to identify the vehicles and determine the beamformer associated with a given vehicle. After the initialization phase, predictive beamforming is performed for downlink data transmission from the RSU to the vehicles. In particular, based on ISAC, the sensing information obtained

<sup>8</sup>The total power constraint, i.e.,  $\sum_{k=1}^K \|\mathbf{f}_{k,n}\|^2 \leq P$ , is another widely adopted option to limit the power consumption at the RSU. Our proposed schemes can be extended to the case where the total power constraint is used.

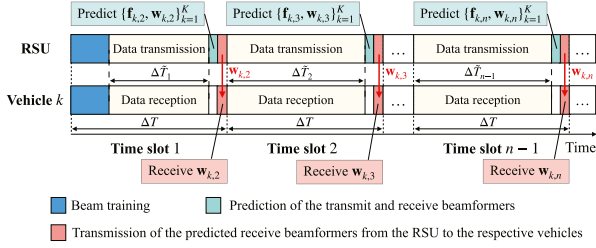


Fig. 3. Time frame structure of the ISAC-enabled OSPB scheme. In time slot 1, the communication links between the RSU and vehicles are established through beam training. After data transmission, the RSU predicts the transmit and receive beamformers for the next time slot based on the reflected sensing signals. Then, the RSU forwards the predicted receive beamformer to each vehicle at the end of time slot 1. In the subsequent time slots, the RSU and vehicles maintain the communication links by using the beamforming vectors obtained in the previous time slot.

from the reflected sensing signals in (9) can be exploited to facilitate beamformer prediction and enhance the communication performance in terms of the achievable sum-rate. In this section, we consider the case where the vehicles have limited computational resources and propose an OSPB scheme for the RSU to predict both the transmit and receive beamformers. In the following, we first introduce the time frame structure of the proposed OSPB scheme. We then develop the corresponding deep learning based predictive model.

#### A. Time Frame Structure of OSPB Scheme

The time frame structure of the proposed ISAC-enabled OSPB scheme is shown in Fig. 3. In time slot 1, the communication links are first established through beam training, during which the transmit beamformer  $\{\mathbf{f}_{k,1}\}_{k=1}^K$  for the RSU and the receive beamformers  $\mathbf{w}_{k,1}$  for the  $k$ -th vehicle can be obtained.<sup>9</sup> Then, the RSU transmits downlink signals to the vehicles and receives the reflected sensing signals simultaneously. In the subsequent time slots, the RSU predicts both the transmit and receive beamformers based on the reflected sensing signals. In particular, to maintain the communication links in time slot  $n$ , the RSU predicts the beamformers  $\{\mathbf{f}_{k,n}, \mathbf{w}_{k,n}\}_{k=1}^K$  in time slot  $n-1$  through a predictive model. The design of the predictive model will be presented in the next subsection. Then, the RSU forwards the predicted receive beamformers  $\{\mathbf{w}_{k,n}\}_{k=1}^K$  to the respective vehicles at the end of time slot  $n-1$ . In time slot  $n$ , the RSU communicates with the vehicles using transmit beamformer  $\{\mathbf{f}_{k,n}\}_{k=1}^K$ , which was predicted in time slot  $n-1$ , and the  $k$ -th vehicle utilizes the receive beamformer  $\mathbf{w}_{k,n}$ , which was obtained from the RSU in time slot  $n-1$ .

<sup>9</sup>We note that various codebook-based approaches can be employed for beam training, such as exhaustive search and hierarchical search. For mmWave channels, where the coherence time is on the orders of milliseconds corresponding to hundreds of symbols, beam training can be completed based on tens to one hundred pilot symbols, which is well within one coherence time interval. In this paper, similar to other state-of-the-art works [12], [13], [14], [15], we assume the initialization phase has been completed. We focus on the subsequent predictive beamforming for vehicle tracking.

#### B. Proposed Deep Learning Based Algorithm for OSPB Scheme

Given the time frame structure described in the previous subsection, we reformulate problem (15) in an end-to-end manner, where the RSU predicts the transmit and receive beamformers directly from the previously received sensing signals in (9) without estimating the channel matrix  $\mathbf{H}_{k,n}$ ,  $k = 1, \dots, K$ . In particular, we aim to find a predictive model  $f(\cdot)$ , which maps the received sensing signals in time slot  $n-1$  to the predictive transmit and receive beamformers in order to maximize the achievable sum-rate in time slot  $n$ . In time slot  $n-1$ , the RSU collects the reflected sensing signals from all vehicles based on (9) in matrix  $\mathbf{\Gamma}_{n-1} = [\bar{\mathbf{r}}_{1,n-1} \dots \bar{\mathbf{r}}_{K,n-1}]^T \in \mathbb{C}^{K \times N_r}$ . We use 3-D tensor  $\mathbf{\Gamma}_{n-1}^\tau = \{\mathbf{\Gamma}_{n-\tau} \dots \mathbf{\Gamma}_{n-1}\} \in \mathbb{C}^{\tau \times K \times N_r}$  to denote the reflected sensing signals received in the previous  $\tau$  time slots, i.e., from time slot  $n-\tau$  to time slot  $n-1$ . To maximize the achievable sum-rate in time slot  $n$ , we reformulate the predictive beamforming problem as follows:

$$\underset{f(\cdot)}{\text{maximize}} \sum_{k=1}^K \log_2(1 + \gamma_{k,n}(\mathbf{f}_{k,n}, \mathbf{w}_{k,n})) \quad (16a)$$

$$\text{subject to } \{\mathbf{f}_{k,n}, \mathbf{w}_{k,n}\}_{k=1}^K = f(\mathbf{\Gamma}_{n-1}^\tau). \quad (16b)$$

Constraint (16b) indicates that transmit beamformer  $\{\mathbf{f}_{k,n}\}_{k=1}^K$  of the RSU, and receive beamformer  $\{\mathbf{w}_{k,n}\}_{k=1}^K$  of vehicle,  $k = 1, \dots, K$ , are obtained from predictive model  $f(\cdot)$  based on the reflected sensing signals  $\mathbf{\Gamma}_{n-1}^\tau$ .

The sum-rate objective function in problem (16) is non-convex, which makes the problem challenging to solve. Various optimization-based methods (e.g., ZF and MMSE beamforming) have been developed to obtain a suboptimal solution for the transmit and receive beamformers. However, the conventional algorithms require the RSU to first estimate the channel parameters, which introduces additional overhead. Moreover, these suboptimal algorithms suffer from performance degradation as they are not directly targeting the ultimate objective, i.e., sum-rate maximization.

We address these issues by using deep learning based schemes, which have shown great potential for solving non-convex problems due to the universal approximation capability of DNNs. In particular, by characterizing the predictive model  $f(\cdot)$  with a DNN parameterized by  $\Phi$ , i.e.,  $\mathcal{F}(\cdot; \Phi)$ , we reformulate problem (16) as follows:

$$\underset{\Phi}{\text{maximize}} \mathbb{E}_{\{\mathbf{H}_{k,n}\}_{k=1}^K} \left\{ \sum_{k=1}^K \log_2(1 + \gamma_{k,n}(\mathbf{f}_{k,n}, \mathbf{w}_{k,n})) \right\} \quad (17a)$$

$$\text{subject to } \{\mathbf{f}_{k,n}, \mathbf{w}_{k,n}\}_{k=1}^K = \mathcal{F}(\mathbf{\Gamma}_{n-1}^\tau; \Phi), \quad (17b)$$

where the expectation  $\mathbb{E}\{\cdot\}$  is taken over the channel matrices  $\{\mathbf{H}_{k,n}\}_{k=1}^K$ . The network parameters  $\Phi$  can be learned in an offline training stage. During training, the expectation in (17a) is replaced by the average achievable sum-rate over a training dataset  $\mathcal{T}_{tr}$ , which is generated based on different channel realizations. When the offline training is completed, the trained network is used for predictive beamforming in an online manner. Using

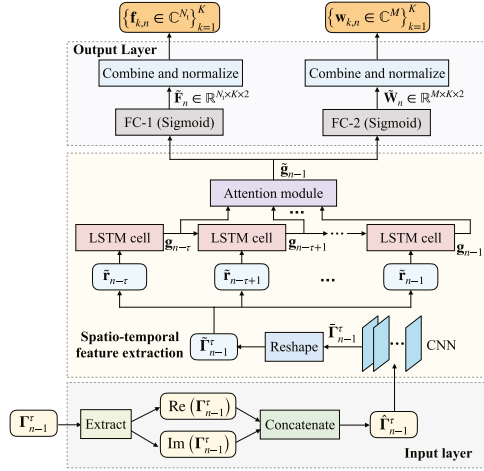


Fig. 4. DNN structure for OSPB scheme.

the reflected sensing signals as input, we obtain the transmit and receive beamformers based on the trained DNN without estimating the CSI.

Since the reflected sensing signals are time sequence data, capturing the temporal correlation in the reflected sensing signals is important for predictive beamformer design. In addition, the DoFs in the spatial domain also play a key role in interference management. In the following, we develop a DNN, which contains CNN, LSTM, and attention modules, to extract both the spatial and temporal features of the reflected sensing signals. The network structure of the proposed DNN for OSPB is shown in Fig. 4 and explained in the following.

1) *Input layer*: Given the reflected sensing signals  $\Gamma_{n-1}^\tau$  with dimension  $\tau \times K \times N_r$ , we extract the real and imaginary parts of  $\Gamma_{n-1}^\tau$ , and obtain  $\text{Re}(\Gamma_{n-1}^\tau)$  and  $\text{Im}(\Gamma_{n-1}^\tau)$ , respectively. We concatenate the real and imaginary parts and form a 4-D input tensor  $\hat{\Gamma}_{n-1}^\tau \in \mathbb{R}^{\tau \times 2 \times K \times N_r}$ .

2) *CNN*: We adopt a CNN module to extract the spatial features of the reflected sensing signals in each time slot. The real and imaginary parts of the sensing signals are regarded as two input channels for convolution. We adopt a 2-D convolutional filter with kernel size  $3 \times 3$ , stride 1, and zero padding. The number of output channels is given by  $H$ . After convolution, we obtain the processed sensing signals  $\tilde{\Gamma}_{n-1}^\tau \in \mathbb{R}^{\tau \times H \times C_1 \times C_2}$ , where  $C_1$  and  $C_2$  are the dimensions after the convolutional operation. The parameters of the convolutional filter of the CNN are denoted as  $\Phi_{\text{CNN}}$ .

3) *LSTM network*: After the convolutional operation, we reshape the tensor  $\tilde{\Gamma}_{n-1}^\tau$  into a matrix  $\tilde{\mathbf{F}}_{n-1}^\tau$  with dimension  $\tau \times HC_1C_2$ . Then, we obtain  $\tilde{\mathbf{F}}_{n-1}^\tau = [\tilde{\mathbf{r}}_{n-\tau} \cdots \tilde{\mathbf{r}}_{n-1}]^T$ , where  $\tilde{\mathbf{r}}_l \in \mathbb{R}^{HC_1C_2}$ . Each row in  $\tilde{\mathbf{F}}_{n-1}^\tau$  is denoted as  $\tilde{\mathbf{r}}_l^T$ , where  $l = n - \tau, \dots, n - 1$ . The LSTM network can capture both the short-term and long-term dependencies in  $[\tilde{\mathbf{r}}_{n-\tau} \cdots \tilde{\mathbf{r}}_{n-1}]^T$ . Each LSTM cell takes the concatenated reflected sensing signals  $\tilde{\mathbf{r}}_l, l = n - \tau, \dots, n - 1$ , as input, and generates the hidden state vector  $\mathbf{g}_l$  based on the following operations:

$$\mathbf{f}_l = \sigma(\mathbf{W}_f \tilde{\mathbf{r}}_l + \mathbf{U}_f \mathbf{g}_{l-1} + \mathbf{b}_f), \quad (18a)$$

$$\mathbf{i}_l = \sigma(\mathbf{W}_i \tilde{\mathbf{r}}_l + \mathbf{U}_i \mathbf{g}_{l-1} + \mathbf{b}_i), \quad (18b)$$

$$\mathbf{o}_l = \sigma(\mathbf{W}_o \tilde{\mathbf{r}}_l + \mathbf{U}_o \mathbf{g}_{l-1} + \mathbf{b}_o), \quad (18c)$$

$$\tilde{\mathbf{c}}_l = \tanh(\mathbf{W}_c \tilde{\mathbf{r}}_l + \mathbf{U}_c \mathbf{g}_{l-1} + \mathbf{b}_c), \quad (18d)$$

$$\mathbf{c}_l = \mathbf{f}_l \odot \mathbf{c}_{l-1} + \mathbf{i}_l \odot \tilde{\mathbf{c}}_l, \quad (18e)$$

$$\mathbf{g}_l = \mathbf{o}_l \odot \tanh(\mathbf{c}_l), \quad (18f)$$

where  $\sigma(\cdot)$  and  $\tanh(\cdot)$  denote the sigmoid and hyperbolic tangent activation functions, respectively.  $\odot$  represents the Hadamard product. We define the set  $\Phi_{\text{LSTM}} = \{\mathbf{W}_f, \mathbf{W}_i, \mathbf{W}_o, \mathbf{W}_c, \mathbf{U}_f, \mathbf{U}_i, \mathbf{U}_o, \mathbf{U}_c, \mathbf{b}_f, \mathbf{b}_i, \mathbf{b}_o, \mathbf{b}_c\}$ , which includes the weights and biases of the LSTM network. In addition,  $\mathbf{f}_l$ ,  $\mathbf{i}_l$ , and  $\mathbf{o}_l$  are the activation vectors for the forget gate, input gate, and output gate, respectively.  $\mathbf{c}_l$  is the cell state vector. The cell state vector and the activation vectors are the intermediate vectors generated by the LSTM network, which are used to update the hidden state vector  $\mathbf{g}_l$ .

4) *Attention module*: Given the input  $\tilde{\mathbf{F}}_{n-1}^\tau = [\tilde{\mathbf{r}}_{n-\tau} \cdots \tilde{\mathbf{r}}_{n-1}]^T$ , the final hidden state of LSTM  $\mathbf{g}_{n-1}$  contains the temporal correlation extracted from the input. However, using a single vector  $\mathbf{g}_{n-1}$  to represent the temporal correlation extracted from  $[\tilde{\mathbf{r}}_{n-\tau} \cdots \tilde{\mathbf{r}}_{n-1}]^T$  may lead to information loss [34]. To tackle this issue, we apply an attention mechanism to the hidden states  $\mathbf{g}_{n-\tau}, \dots, \mathbf{g}_{n-1}$ , such that those hidden states with more information have larger weights in the output state. The weights are determined by an attention module. In particular, we concatenate the final hidden state  $\mathbf{g}_{n-1}$  with  $\mathbf{g}_l$ , and form vector  $\tilde{\mathbf{g}}_{n-1,l} = [\mathbf{g}_{n-1}^T \mathbf{g}_l^T]^T, l = n - \tau, \dots, n - 1$ . We determine the attention weights,  $a_{n-1,l}$ , using the following softmax operation:

$$a_{n-1,l} = \frac{\exp\{\mathbf{v}^T \tanh(\mathbf{W}_a \tilde{\mathbf{g}}_{n-1,l})\}}{\sum_{k=n-\tau}^{n-1} \exp\{\mathbf{v}^T \tanh(\mathbf{W}_a \tilde{\mathbf{g}}_{n-1,k})\}}, \quad (19)$$

$$l = n - \tau, \dots, n - 1,$$

where  $\mathbf{W}_a$  and  $\mathbf{v}$  are the parameters of the attention operation. We denote the set of parameters of the attention module as  $\Phi_{\text{ATT}} = \{\mathbf{W}_a, \mathbf{v}\}$ . Then, the output of the attention module is given by the weighted hidden state vector  $\tilde{\mathbf{g}}_{n-1}$ :

$$\tilde{\mathbf{g}}_{n-1} = \sum_{l=n-\tau}^{n-1} a_{n-1,l} \mathbf{g}_l. \quad (20)$$

5) *Fully-connected (FC) layer*: We use FC-1 and FC-2 to process the extracted spatio-temporal features and generate the transmit and receive beamforming matrices. The outputs of FC-1 and FC-2 are given by  $\tilde{\mathbf{F}}_n \in \mathbb{R}^{N_t \times K \times 2}$  and  $\tilde{\mathbf{W}}_n \in \mathbb{R}^{M \times K \times 2}$ , which include the real and imaginary parts of the obtained transmit and receive beamformers, respectively. The sigmoid function is used as the activation function. We use  $\Phi_{\text{FC}}$  to denote the parameters of the FC network.

6) *Combine and normalize*: We combine the real and imaginary parts of the outputs  $\tilde{\mathbf{F}}_n$  and  $\tilde{\mathbf{W}}_n$  obtained from FC-1 and FC-2, respectively. The transmit and receive beamforming matrices after combination are denoted as  $\hat{\mathbf{F}}_n \in \mathbb{C}^{N_t \times K}$  and  $\hat{\mathbf{W}}_n \in \mathbb{C}^{M \times K}$ , respectively, and are given as follows:

$$\hat{\mathbf{F}}_n = \tilde{\mathbf{F}}_n[:, :, 1] + j\tilde{\mathbf{F}}_n[:, :, 2], \quad (21)$$







$\{\Gamma_{n-\tau} \cdots \Gamma_{n-1}\} \in \mathbb{C}^{\tau \times K \times N_r}$ . On the other hand, the receive beamformer  $\mathbf{w}_{k,n}$  is predicted by the  $k$ -th vehicle locally based on its previously employed beamformer  $\mathbf{w}_{k,n-1}$  in time slot  $n-1$ .

The TSPB scheme has two distinct advantages. First, the RSU only needs to transmit the predictive model to the vehicles once, which is after the beam training stage. There is no need for the RSU to inform the vehicles of their receive beamformers in the subsequent time slots. Second, the predictive model for the vehicles is pre-determined offline and stored at the RSU, without the involvement of the vehicles. This can reduce the computational burden for the vehicles.

### B. Proposed Deep Learning Based Algorithm for TSPB Scheme

Based on the time frame structure of the TSPB scheme, we aim to find the predictive models, i.e.,  $f_R(\cdot)$  and  $f_V(\cdot)$ , for the RSU and vehicles, respectively. At the RSU side, the predictive model takes the reflected sensing signals from time slot  $n-\tau$  to time slot  $n-1$ , i.e.,  $\Gamma_{n-1}^\tau = \{\Gamma_{n-\tau} \cdots \Gamma_{n-1}\} \in \mathbb{C}^{\tau \times K \times N_r}$ , as input and determines the transmit beamformer. The predictive model at the  $k$ -th vehicle takes  $\mathbf{w}_{k,n-1}$  as input and determines its receive beamformer  $\mathbf{w}_{k,n}$  for time slot  $n$ . To maximize the achievable sum-rate in time slot  $n$ , the predictive beamforming problem is formulated as follows:

$$\underset{f_R(\cdot), f_V(\cdot)}{\text{maximize}} \sum_{k=1}^K \log_2(1 + \gamma_{k,n}(\mathbf{f}_{k,n}, \mathbf{w}_{k,n})) \quad (28a)$$

$$\text{subject to } \{\mathbf{f}_{k,n}\}_{k=1}^K = f_R(\Gamma_{n-1}^\tau), \quad (28b)$$

$$\mathbf{w}_{k,n} = f_V(\mathbf{w}_{k,n-1}), \quad k = 1, \dots, K. \quad (28c)$$

Different from problem (16), problem (28) aims to determine the two models which are used for transmit and receive beamformer prediction, respectively. Compared with problem (16), here the receive beamformers are determined by the vehicles themselves, without relying on the downlink signaling information from the RSU. Similarly, we characterize the predictive models  $f_R(\cdot)$  and  $f_V(\cdot)$  with DNNs parameterized by  $\Phi_R$  and  $\Phi_V$ , i.e.,  $\mathcal{F}_R(\cdot; \Phi_R)$  and  $\mathcal{F}_V(\cdot; \Phi_V)$ , respectively. Then, we reformulate problem (28) for the communication in time slot  $n$  as follows:

$$\underset{\Phi_R, \Phi_V}{\text{maximize}} \mathbb{E}_{\{\mathbf{H}_{k,n}\}_{k=1}^K} \left\{ \sum_{k=1}^K \log_2(1 + \gamma_{k,n}(\mathbf{f}_{k,n}, \mathbf{w}_{k,n})) \right\} \quad (29a)$$

$$\text{subject to } \{\mathbf{f}_{k,n}\}_{k=1}^K = \mathcal{F}_R(\Gamma_{n-1}^\tau; \Phi_R), \quad (29b)$$

$$\mathbf{w}_{k,n} = \mathcal{F}_V(\mathbf{w}_{k,n-1}; \Phi_V), \quad k = 1, \dots, K. \quad (29c)$$

The DNNs' parameters  $\Phi_R$  and  $\Phi_V$  can be learned in an offline training stage. During training, these two DNNs are jointly trained at the RSU side in an unsupervised manner to directly maximize the achievable sum-rate, where the vehicles are not involved in the training stage. In the following, we present the network structures for  $\mathcal{F}_R(\cdot; \Phi_R)$  and  $\mathcal{F}_V(\cdot; \Phi_V)$ .

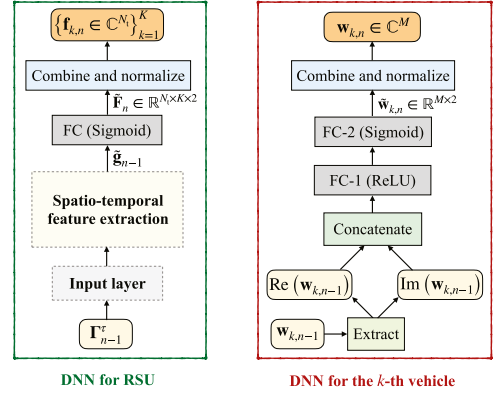


Fig. 6. DNNs structure for TSPB scheme.

For transmit beamformer design at the RSU, similar to the OSPB scheme, we propose to extract the spatio-temporal features in the reflected sensing signals through CNN, LSTM, and attention modules. The DNN for RSU is illustrated on the left-hand side of Fig. 6. The spatio-temporal feature extraction follows similar steps as shown in Steps 1)–4) in Section II-B. In particular, the input to the DNN at the RSU is given by  $\Gamma_{n-1}^\tau = \{\Gamma_{n-\tau} \cdots \Gamma_{n-1}\} \in \mathbb{C}^{\tau \times K \times N_r}$ , which contains the reflected sensing signals from time slot  $n-\tau$  to time slot  $n-1$ . The DNN extracts the spatio-temporal features and obtains  $\tilde{\mathbf{g}}_{n-1}$ . Then, we use an FC layer to obtain the real and imaginary parts of the transmit beamformer, i.e.,  $\hat{\mathbf{F}}_n \in \mathbb{R}^{N_t \times K \times 2}$ . We combine the real and imaginary parts to obtain the beamforming matrix  $\hat{\mathbf{F}}_n = [\hat{\mathbf{f}}_{1,n} \cdots \hat{\mathbf{f}}_{K,n}]$  from (21), where the  $k$ -th column of  $\hat{\mathbf{F}}_n$  denotes the transmit beamforming vector for the  $k$ -th vehicle. Then, we normalize each  $\hat{\mathbf{f}}_{k,n}$  and obtain  $\mathbf{f}_{k,n}$  as in (23) to satisfy the power constraint at the RSU. We denote the parameters of the DNN at the RSU as  $\Phi_R$ . For the receive beamformer design at the  $k$ -th vehicle, we apply two FC layers to map the input, i.e.,  $\mathbf{w}_{k,n-1}$  to the predictive receive beamformer  $\mathbf{w}_{k,n}$  in time slot  $n$ . The DNN structure for the  $k$ -th vehicle is shown on the right-hand side of Fig. 6. The rectified linear unit (ReLU) is used as activation function for hidden layer FC-1 and the sigmoid activation function is used for output layer FC-2. The weights and biases of the DNN used by the vehicles correspond to parameters  $\Phi_V$ . For the  $k$ -th vehicle, the output of FC-2 is given by  $\tilde{\mathbf{w}}_{k,n} \in \mathbb{R}^{M \times 2}$ , which includes the real and imaginary parts of the predicted receive beamformer. Similarly, we combine the real and imaginary parts to obtain  $\hat{\mathbf{w}}_{k,n} \in \mathbb{C}^M$  as follows:

$$\hat{\mathbf{w}}_{k,n} = \tilde{\mathbf{w}}_{k,n}[:, 1] + j\tilde{\mathbf{w}}_{k,n}[:, 2], \quad k = 1, \dots, K. \quad (30)$$

Then, we normalize  $\hat{\mathbf{w}}_{k,n}$  and obtain the receive beamformer  $\mathbf{w}_{k,n}$  for the  $k$ -th vehicle via (24).

Given the DNNs for the RSU and the vehicles, the loss function can be expressed as

$$\begin{aligned} \mathcal{L}(\{\mathbf{f}_{k,n}, \mathbf{w}_{k,n}\}_{k=1}^K; \Phi_R, \Phi_V) \\ = - \sum_{k=1}^K \log_2(1 + \gamma_{k,n}(\mathbf{f}_{k,n}, \mathbf{w}_{k,n})). \end{aligned} \quad (31)$$

These two DNNs are jointly trained at the RSU in an unsupervised manner to minimize the loss function in (31) using Adam optimizer [35]. We construct a dataset  $\mathcal{T}_{\text{tr}}$  for DNN training, which contains  $N_{\text{tr}}$  data samples, i.e.,  $\mathcal{T}_{\text{tr}} = \{(\mathbf{I}_{n-1}^{(1)}, \mathbf{W}_{n-1}^{(1)}, \mathbf{H}_n^{(1)}), \dots, (\mathbf{I}_{n-1}^{(N_{\text{tr}})}, \mathbf{W}_{n-1}^{(N_{\text{tr}})}, \mathbf{H}_n^{(N_{\text{tr}})})\}$ , in which  $\mathbf{H}_n^{(i)} = \{\mathbf{H}_{1,n}^{(i)}, \dots, \mathbf{H}_{K,n}^{(i)}\}$ ,  $i = 1, \dots, N_{\text{tr}}$ . After training, we obtain the trained DNNs with parameters  $\Phi_{\text{R}}^*$  and  $\Phi_{\text{V}}^*$ , and perform online predictive beamforming. During the online predictive beamforming, each vehicle first downloads the trained network parameters  $\Phi_{\text{V}}^*$  from the RSU. Then, given the testing data in time slot  $n - 1$ , i.e., the reflected sensing signals  $\mathbf{I}_{n-1}^{(\text{ts})}$ , the RSU can predict the transmit beamformer  $\{\mathbf{f}_{k,n}^{(\text{ts})}\}_{k=1}^K$  for time slot  $n$ . The  $k$ -th vehicle can determine its predictive beamformer  $\mathbf{w}_{k,n}^{(\text{ts})}$  based on the previously employed beamformer  $\mathbf{w}_{k,n-1}^{(\text{ts})}$  through the downloaded DNN without estimating the CSI.

### C. Computational Complexity Analysis

In this subsection, we provide a computational complexity analysis for the developed deep learning based algorithm for the TSPB scheme. For the computational complexity, we begin with the offline training stage. The offline training is performed at the RSU, and the computational complexity includes the computation of two DNNs. For the DNN at the RSU, the computational complexity includes the CNN, LSTM, attention, and FC modules, which is given by  $\mathcal{O}(\tau(S^2 H C_1 C_2 + D_i D_o + D_o^2) + D_o K N_t)$ .  $S, H, C_1, C_2, D_i$ , and  $D_o$  follow the same notations introduced in Section III-C. The DNN deployed at each vehicle comprises two FC layers, with weights being  $M \times D_f$  and  $D_f \times M$ , respectively.  $D_f$  denotes the dimension of the output of the FC-1 layer. The computational complexity is given by  $\mathcal{O}(M D_f)$ . The overall computational complexity for offline unsupervised training  $C_{\text{off}}$  can be expressed as

$$C_{\text{off}} = \mathcal{O}\left(N_{\text{tr}} (\tau(S^2 H C_1 C_2 + D_i D_o + D_o^2) + D_o K N_t + K M D_f)\right). \quad (32)$$

For online beamforming, the RSU needs to compute the transmit beamformer and the corresponding computational complexity is given by

$$C_{\text{on}}^{\text{R}} = \mathcal{O}(\tau(S^2 H C_1 C_2 + D_i D_o + D_o^2) + D_o K N_t). \quad (33)$$

For each vehicle, the computational complexity is dominated by the FC layers for receive beamformer design and is given by

$$C_{\text{on}}^{\text{V}} = \mathcal{O}(M D_f). \quad (34)$$

From (34), we observe that the computational complexity for each vehicle is linear with respect to the number of antennas  $M$  and also depends on the number of parameters of the proposed DNN.

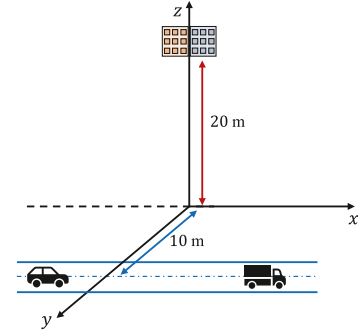


Fig. 7. The 3-D coordinate system setting.

## V. PERFORMANCE EVALUATION

### A. System Setting and Baseline Schemes

In this section, we evaluate the performance of the proposed OSPB and TSPB schemes. Unless stated otherwise, the RSU has  $N_t = 256$  ( $N_h^{(\text{tx})} = 16$ ,  $N_v^{(\text{tx})} = 16$ ) transmit antennas and  $N_r = 256$  ( $N_h^{(\text{rx})} = 16$ ,  $N_v^{(\text{rx})} = 16$ ) receive antennas. The RSU serves  $K = 4$  vehicles on a single-lane road. Each vehicle is equipped with an  $8 \times 8$  UPA. The system is operated at a carrier frequency of 30 GHz. The path loss exponent  $\zeta$  is set to 3.6. The radar cross-section follows a Gaussian distribution with a mean value of  $10 \text{ m}^2$  and a standard deviation of  $8 \text{ m}^2$ . We set  $\sigma_c^2$  to be  $-80 \text{ dBm}$ . The reference distance  $d_0$  is set to  $1 \text{ m}$  and the path loss at the reference distance is given by  $\alpha_0 = -60 \text{ dB}$ . Similar to [12], [13], [15], we set  $\sigma_r^2 = -60 \text{ dBm}$  and  $\xi = 10$  for the observed reflected signal samples after delay and Doppler frequency compensation. Consider a 3-D environment based on an  $xyz$ -coordinate system, as shown in Fig. 7. The UPAs of the RSU are deployed at an altitude of  $20 \text{ m}$ . Without loss of generality, the UPAs of the RSU are located at coordinate  $[0, 0, 20] \text{ m}$ . For simplicity, we assume the UPAs of the RSU are not tilted. The single-lane road is located on the line  $y = 10 \text{ m}$  in the  $xy$ -plane, and the vehicles move along the single-lane road. The initial positions of the vehicles are randomly located on the road within a range of  $-25 \sim 25 \text{ m}$  on the  $x$ -axis. The distance between two adjacent vehicles is between  $10 \text{ m}$  and  $14 \text{ m}$ . The initial speed of each vehicle is randomly generated from a uniform distribution between  $8 \text{ m/s}$  and  $12 \text{ m/s}$ . The duration of each time slot  $\Delta T$  is set to  $0.02 \text{ s}$ . We set  $\tau$  to be equal to 4. Based on this system setting, we generated 5,000 samples, where 4,000 of them are used for training and the remaining 1,000 samples are used for testing. The following results are obtained by averaging 1,000 Monte Carlo realizations in the testing set. The learning rate of the Adam optimizer for unsupervised training is set to  $10^{-3}$ . For the DNN of the OSPB scheme, the CNN has 16 output channels and the kernel size is set to  $3 \times 3$ . The hidden size of the LSTM and attention layer is set to 2,048. For the output layer, the beamformers are generated through two FC layers. For the DNN of the TSPB scheme, the RSU employs a similar network as the OSPB scheme. The DNN at the vehicle side generates the receive beamformer through two FC layers, with weights being  $M \times 256$  and  $256 \times M$ , respectively.

For performance comparison, we consider seven baseline schemes. In particular, we consider three conventional beamforming design with perfect CSI as the baselines. Furthermore, we adopt the algorithms proposed in [12] and [15] for comparison purposes. To evaluate the effectiveness of our proposed DNNs, we also compare them with two simple DNN structures based on the OSPB scheme. The seven baseline schemes are as follows:

- **MMSE beamforming with perfect CSI:** We assume the channel matrices  $\mathbf{H}_{k,n}$ ,  $k = 1, \dots, K$ , are perfectly known by the RSU and each vehicle. At each vehicle, the beam steering vector  $\mathbf{u}(\varphi_{k,n}, \vartheta_{k,n})$ ,  $k = 1, \dots, K$ , is used for receive beamforming to improve the beamforming gain. At the RSU, MMSE beamforming is adopted.
- **ZF beamforming with perfect CSI:** This scheme is also based on the assumption that the channel matrices are perfectly known by the RSU and each vehicle. Each vehicle uses its beam steering vector, i.e.,  $\mathbf{u}(\varphi_{k,n}, \vartheta_{k,n})$ ,  $k = 1, \dots, K$ , to receive the downlink signals and the RSU employs ZF beamforming.
- **SVD-based beamforming with perfect CSI:** Perfect CSI is assumed to be available at the RSU and vehicles. Based on the SVD method, the channel matrix of each vehicle, i.e.,  $\mathbf{H}_{k,n}$ ,  $k = 1, \dots, K$ , can be factorized as  $\mathbf{H}_{k,n} = \mathbf{G}_{k,n} \mathbf{\Sigma}_{k,n} \mathbf{Q}_{k,n}^H$ , where  $\mathbf{G}_{k,n}$  and  $\mathbf{Q}_{k,n}$  are the left and right singular vector matrices, and  $\mathbf{\Sigma}_{k,n}$  is a diagonal matrix with the singular values of  $\mathbf{H}_{k,n}$  on the main diagonal. The transmit and receive beamformers of the  $k$ -th vehicle are given by the first columns of  $\mathbf{Q}_{k,n}$  and  $\mathbf{G}_{k,n}$ , respectively, corresponding to the maximum singular value of  $\mathbf{H}_{k,n}$ .
- **EKF [12]:** The EKF scheme first estimates AoDs  $\{\phi_{k,n}, \theta_{k,n}\}$  and AoAs  $\{\varphi_{k,n}, \vartheta_{k,n}\}$ ,  $k = 1, \dots, K$ , based on a mathematical model, which describes the kinematic relationship between the angle, the speed of the vehicle, and the distance between the vehicle and the RSU. The transmit and receive beamformers are then given by the beam steering vectors, i.e.,  $\mathbf{a}(\phi_{k,n}, \theta_{k,n})$  and  $\mathbf{u}(\varphi_{k,n}, \vartheta_{k,n})$ ,  $k = 1, \dots, K$ , respectively, based on the estimated angles.
- **E-HCL:** Here, we extend the HCL-Net approach proposed in [15], where each vehicle is equipped with a single antenna, to the E-HCL scheme addressing both transmit and receive beamforming. The HCL-Net takes the estimated historical CSI as input and predicts the transmit beamformer for the RSU. When a UPA is deployed at each vehicle, the CSI between the RSU and each vehicle becomes a matrix instead of a vector. For the E-HCL scheme, we make the following two changes to the HCL-Net approach. We assume the AoA is known by each vehicle, and the vehicles set their corresponding receive beamformers equal to the beam steering vectors. By multiplying the receive beamformer with the channel matrix, we obtain an effective channel vector for each vehicle. The E-HCL network takes the historical effective channel vectors as the input. For the output layer, HCL-Net uses an FC layer to determine the transmit beamformer, while E-HCL uses two separate FC layers to generate both the transmit and

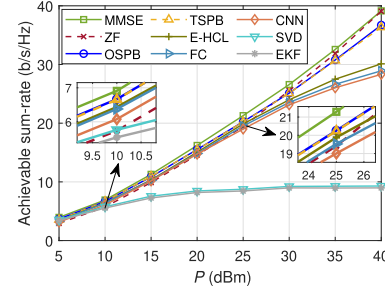


Fig. 8. Achievable sum-rate versus the maximum transmit power  $P$  ( $K = 4$ ,  $N_t = N_r = 256$ ,  $M = 64$ ).

receive beamformers. For the presented simulation results, we assume perfect CSI knowledge for the E-HCL scheme.

- **FC:** This network uses three FC layers to process the reflected sensing signals and predict the transmit and receive beamformers. The number of neurons in each layer is given by 512, 1,024, and 2,048, respectively. The ReLU is employed as the activation function. Based on the OSPB scheme, the network takes the reflected sensing signals as input and provides the transmit and receive beamformers as output.
- **CNN:** This DNN structure includes a 2-layer CNN followed by an FC layer. Max-pooling is performed on each CNN layer. The number of channels in each CNN layer is set to 32. The number of neurons in the FC layer is set to 2,048. Given the reflected sensing signals, the network outputs the transmit and receive beamformers.

## B. Performance Comparison

In Fig. 8, we show the achievable sum-rate versus the maximum transmit power  $P$  at the RSU. We observe that when the transmit power is low (i.e.,  $P \leq 10$  dBm), all considered schemes achieve similar performance and can guarantee an achievable sum-rate of over 5b/s/Hz. This demonstrates that all schemes provide considerable beamforming gains to combat path loss and noise. As the transmit power increases, the SVD-based beamforming and EKF approach tend to saturate quickly. This is because in the high transmit power regime, inter-vehicle interference becomes the dominating factor affecting the achievable sum-rate. The SVD-based beamforming does not account for inter-vehicle interference. The EKF scheme predicts the spatial angles of the vehicles only and may not be able to fully mitigate the interference among vehicles. On the other hand, the proposed OSPB and TSPB schemes can further improve the sum-rate performance and approach to the performance achieved by MMSE beamforming with perfect CSI. The proposed OSPB and TSPB schemes always outperform the EKF algorithm, demonstrating the benefits of predicting the beamformers in an end-to-end manner and the effectiveness in interference management. Moreover, although perfect CSI is assumed to be available for the E-HCL network, our proposed schemes still achieve better performance, which underscores the effectiveness of the developed DNN structures.



Similar conclusions can be drawn when comparing the proposed schemes with the FC and CNN structures. Given the numerical results in Fig. 8, we summarize the advantages of the proposed OSPB and TSPB schemes as follows:

- The proposed schemes directly address the ultimate goal, i.e., maximizing the achievable sum-rate. The EKF scheme first estimates the state parameters using distance metrics (i.e., Euclidean distance), and the unavoidable estimation error can impact the subsequent beamforming design. This may lead to a degradation of the sum-rate due to error propagation. Our proposed schemes tackle this issue by eliminating the intermediate estimation phase, thus further enhancing the overall sum-rate performance.
- The proposed DNNs have a strong capability to capture the spatio-temporal features of the reflected sensing signals and approximate the non-convex objective function in problems (16) and (28). Compared with the E-HCL, FC, and CNN schemes, the proposed schemes have a higher flexibility in jointly designing the transmit and receive beamformers for sum-rate maximization, which yields a better suboptimal solution than the other DNN structures considered.

When comparing between the proposed OSPB and TSPB schemes, we observe that both schemes achieve a similar sum-rate. This is because the structures of the proposed DNNs used for the spatio-temporal feature extraction in both schemes are similar. In the OSPB scheme, the transmit and receive beamformers are jointly obtained at the RSU via a single DNN, and the spatio-temporal features are extracted based on the reflected sensing signals. In the TSPB scheme, while the transmit and receive beamformers are respectively determined via two DNNs, both DNNs are jointly trained at the RSU. Therefore, the trained DNNs can extract the spatio-temporal features based on both the reflected sensing signals and the previously employed receive beamformers. The slight difference in the achievable sum-rate of both schemes can be attributed to the fact that the DNNs for TSPB require the previously employed receive beamformers as input whereas the DNN for OSPB does not. The random initializations of the DNNs during the training stage can also affect the training and testing performance.

In Fig. 9(a) and (b), the impact of the UPA architecture at the RSU is studied. The total number of antennas of the transmit UPA is set to  $N_t = 256$  and 64, respectively. In each setting, we set the ratio of the number of horizontal antennas to the number of vertical antennas, i.e.,  $N_h^{(tx)} : N_v^{(tx)}$ , to 4 : 1, 1 : 1, and 1 : 4, respectively. The receive UPA has the same architecture as the transmit UPA, i.e.,  $N_h^{(rx)} = N_h^{(tx)}$  and  $N_v^{(rx)} = N_v^{(tx)}$ . The results in Fig. 9 reveal that, for a given ratio  $N_h^{(tx)} : N_v^{(tx)}$ , all considered schemes yield a higher achievable sum-rate if the number of antennas is increased, as additional antennas can improve the beamforming gain by providing more DoFs in the spatial domain. Moreover, given a fixed total number of antennas, it can be observed that the horizontal antennas play a more significant role than the vertical antennas. Since the vehicles move in the same horizontal plane, increasing the number of horizontal antennas enhances the capability of

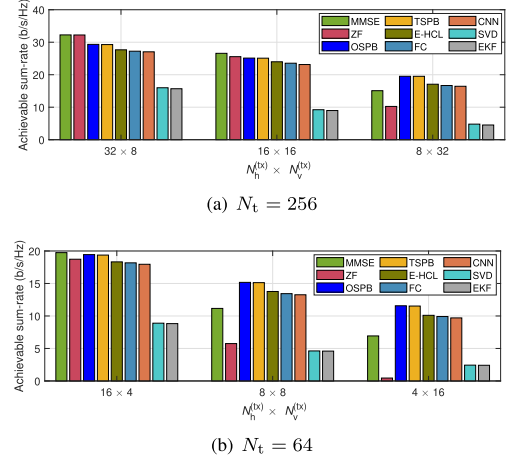


Fig. 9. Achievable sum-rate for different UPA architectures at the RSU ( $P = 30$  dBm,  $K = 4$ ,  $N_h^{(rx)} = N_h^{(tx)}$ ,  $N_v^{(rx)} = N_v^{(tx)}$ ,  $M = 64$ ).

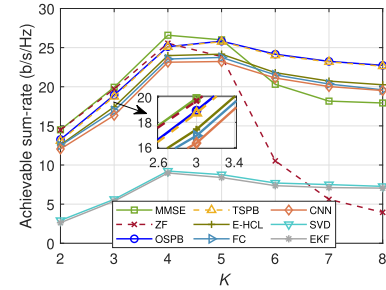


Fig. 10. Achievable sum-rate versus the number of vehicles  $K$  ( $P = 30$  dBm,  $N_t = N_r = 256$ ,  $M = 64$ ).

the RSU to distinguish different vehicles and manage inter-vehicle interference. Furthermore, when  $N_h^{(tx)} : N_v^{(tx)}$  is equal to 1 : 4, the proposed OSPB and TSPB schemes outperform the MMSE beamforming approach. This is because the proposed schemes jointly design the transmit and receive beamformers, resulting in a more effective strategy for interference management.

In Fig. 10, we evaluate the impact of the number of vehicles  $K$  on the achievable sum-rate. From the results, we observe that when  $K \leq 4$ , the achievable sum-rate increases as the number of vehicles increases for all considered schemes. This is because a higher number of vehicles enhances the diversity gain in the spatial domain. When the number of vehicles continues to increase further, the sum-rate begins to decrease.<sup>10</sup> This is due to the fact that as the number of vehicles increases, the transmit power allocated to each vehicle decreases and the channels of the vehicles also become more mutually correlated, such that the mutual interference between the vehicles becomes more severe. Moreover, it can be observed that when  $K \geq 6$ , the performance of the ZF beamformer drops significantly. The main reason for this is that an increase in  $K$  reduces the dimension of the null space of the vehicles' channels. As the vehicles'

<sup>10</sup>We assume that all  $K$  vehicles are always scheduled.

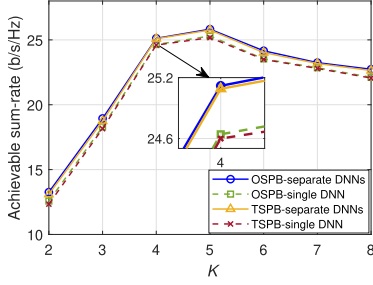


Fig. 11. Achievable sum-rate versus the number of vehicles  $K$  ( $P = 30$  dBm,  $N_t = N_r = 256$ ,  $M = 64$ ,  $K_{\max} = 8$ ).

channels become strongly correlated, the  $N_t$  transmit antennas at the RSU become insufficient to fully null the mutual interference, such that the overall performance degrades. In addition, since beam steering is employed by the vehicles for receive beamforming, the antenna arrays of the vehicles do not contribute to interference mitigation. Similarly, the performance of the MMSE beamformer also degrades since it cannot effectively mitigate the interference. Thus, when  $K \geq 6$ , the proposed schemes outperform MMSE beamforming due to the joint design of the transmit and receive beamformers, providing better flexibility in managing inter-vehicle interference.

### C. Adjustment to Different Numbers of Vehicles

For the simulation results presented in the previous subsection, the DNNs are trained with a given number of vehicles. When the number of vehicles varies, separate DNN models need to be trained, each targeting a specific number of vehicles. While using separate DNN models for different numbers of vehicles can guarantee high performance, it also results in a high training complexity. In this subsection, we apply a different training strategy, such that a single trained model can accommodate different numbers of vehicles. In particular, we first set a maximum number of vehicles  $K_{\max}$  that the RSU can serve. During offline training, we train a DNN model on data samples collected for different numbers of vehicles. We note that the input and output sizes of the DNN remain the same for different numbers of vehicles. When the number of vehicles  $K$  is less than  $K_{\max}$ , the input tensor is padded with zero values to reach the required size, i.e.,  $\tau \times K_{\max} \times N_r$ . The first  $K$  outputs are employed as the beamformers to accommodate those  $K$  vehicles which are in the system. In Fig. 11, we show the achievable sum-rate for different values of  $K$ , where we set  $K_{\max} = 8$ . For each  $K \in \{2, 3, \dots, 8\}$ , we generate 3,000 data samples, and thus there are 21,000 data samples in total. We use 80% of data samples for training and we test the predictive beamforming performance on the remaining 20% of data samples. We show the performance achieved with separate DNN models, each targeting a specific number of vehicles, and that achieved with a single DNN model for different numbers of vehicles. Compared to separate DNNs trained for different numbers of vehicles, the results in Fig. 11 indicate that using a single DNN trained on various numbers of vehicles yields comparable performance. Thus, both the OSPB and TSPB schemes with a single trained

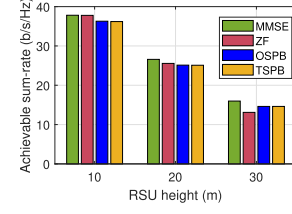


Fig. 12. Impact of the RSU height on the achievable sum-rate ( $K = 4$ ,  $N_t = N_r = 256$ ,  $M = 64$ ).

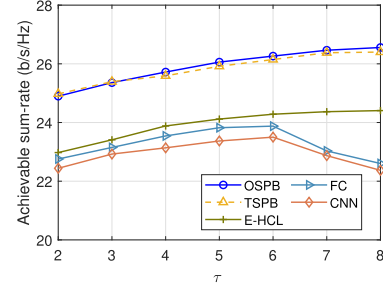


Fig. 13. Achievable sum-rate versus the number of previous time slots  $\tau$ , from which the reflected sensing signals were used for predictive beamforming design ( $P = 30$  dBm,  $K = 4$ ,  $N_t = N_r = 256$ ,  $M = 64$ ).

DNN can still obtain good performance for varying numbers of vehicles.

### D. Performance Evaluation for Different System Settings

In Fig. 12, we evaluate the impact of the height of the RSU on the achievable sum-rate. Our results reveal that lowering the RSU height can improve the achievable sum-rate. Deploying the RSU arrays at a lower height reduces the distance between the RSU and the vehicles, resulting in a larger channel gain. Moreover, a lower RSU height reduces the vertical disparity between the RSU and the vehicles, allowing the beam energy in the vertical domain to be more effectively concentrated on the vehicles.

In Fig. 13, we evaluate the impact of the number of previous time slots,  $\tau$ , from which the reflected sensing signals were used for predictive beamforming design. We include results for the E-HCL, FC, and CNN approaches for performance comparison. The achievable sum-rate for our proposed OSPB and TSPB schemes improves as  $\tau$  increases. This demonstrates the capability of the developed DNNs to capture the temporal features of the reflected sensing signals. Note that the attention module allows the developed DNNs to focus on the most important temporal correlations of the reflected sensing signals, such that the proposed schemes yield a higher achievable sum-rate compared with the E-HCL approach. On the other hand, the FC and CNN models are not able to effectively exploit the temporal correlations when  $\tau > 6$ .

In Fig. 14, we evaluate the impact of noise  $\sigma_r^2$  and the matched-filtering gain  $\xi$  of the reflected sensing signals shown in (9) on the achievable sum-rate. Fig. 14(a) shows that there is an about 20% performance degradation in the achievable

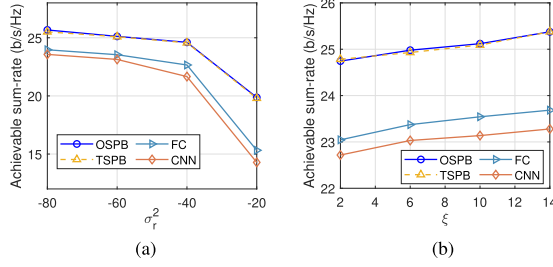


Fig. 14. Effect of (a) noise  $\sigma_r^2$  and (b) matched-filtering gain  $\xi$  of the received sensing signals on the achievable sum-rate ( $P = 30$  dBm,  $K = 4$ ,  $N_t = N_r = 256$ ,  $M = 64$ ).

rate when  $\sigma_r^2$  increases from  $-80$  dBm to  $-20$  dBm. It can be observed that when the noise power in the reflected sensing signals is high (i.e.,  $\sigma_r^2 = -40$  dBm), both schemes can still extract temporal correlation from the reflected sensing signals and predict the beamformers properly. This demonstrates the robustness of the proposed schemes against the noise of the reflected sensing signals. The reasons can be attributed to the capability of the proposed DNNs to handle the uncertainty introduced by noise in the reflected sensing signals. When  $\sigma_r^2$  is equal to  $-20$  dBm, the achievable sum-rate drops significantly due to the fact that the reflected sensing signals are severely corrupted by the noise. From Fig. 14(b), we can observe that for both schemes, the performance can be improved with a higher  $\xi$ , as the reflected sensing signals with a higher matched-filtering gain  $\xi$  can provide more precise information to the DNNs. In both figures, we can observe that the proposed schemes always outperform the other two deep learning based schemes, which confirms again the advantages of our proposed DNN models.

#### E. Effect of Multipath Components

In this subsection, we evaluate the impact of multipath components on the achievable performance. For the communication channel, we consider a spatial channel model [6], which accounts for both the LoS and non-LoS links. The multipath channel between the RSU and the  $k$ -th vehicle in time slot  $n$ ,  $\tilde{\mathbf{H}}_{k,n}$ , can be expressed as follows:

$$\tilde{\mathbf{H}}_{k,n} = \mathbf{H}_{k,n} + \tilde{G} \sum_{l=1}^L \sqrt{\alpha_{k,n}^{(l)}} e^{j\kappa_{k,n}^{(l)}} \times \mathbf{u}(\varphi_{k,n}^{(l)}, \vartheta_{k,n}^{(l)}) \mathbf{a}^H(\phi_{k,n}^{(l)}, \theta_{k,n}^{(l)}), \quad (35)$$

where  $L$  is the number of non-LoS scattering paths.  $\phi_{k,n}^{(l)}$  and  $\theta_{k,n}^{(l)}$  are the azimuth and elevation AoDs of the  $l$ -th path, respectively, which are Laplacian distributed with mean angles  $\{\phi_{k,n}, \theta_{k,n}\}$  and angular spreads  $\{\sigma_\phi, \sigma_\theta\}$ .  $\varphi_{k,n}^{(l)}$  and  $\vartheta_{k,n}^{(l)}$  are the azimuth and elevation AoAs of the  $l$ -th path, respectively, which again are Laplacian distributed with mean angles  $\{\varphi_{k,n}, \vartheta_{k,n}\}$  and angular spreads  $\{\sigma_\varphi, \sigma_\vartheta\}$ .<sup>11</sup> We assume  $\sigma_\phi = \sigma_\theta = \sigma_\varphi = \sigma_\vartheta =$

<sup>11</sup>Here, we model the AoDs/AoAs of the non-LoS paths as Laplacian distributed, with the mean equal to the AoD/AoA of the LoS channel. We note

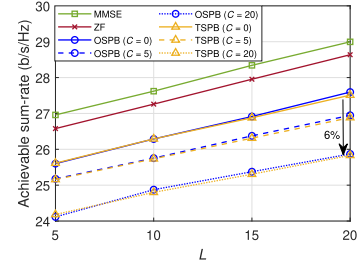


Fig. 15. Effect of multipath components and clutter interference on the achievable sum-rate ( $P = 30$  dBm,  $K = 4$ ,  $N_t = N_r = 256$ ,  $M = 64$ ).

$7.5^\circ$ .  $\alpha_{k,n}^{(l)}$  is the path loss which is defined similarly as  $\alpha_{k,n}$  in (11), i.e.,  $\alpha_{k,n}^{(l)} = \alpha_0 (d_{k,n}^{(l)} / d_0)^{-\zeta^{(l)}}$ , where  $d_{k,n}^{(l)}$  and  $\zeta^{(l)}$  are the distance and path loss exponent of the  $l$ -th non-LoS scattering path, respectively. Given that the angle spreads of the non-LoS paths are small, we have  $d_{k,n}^{(l)} \approx d_{k,n}$  for  $l = 1, \dots, L$ . The path loss exponent  $\zeta^{(l)}$  is set to 4.8, for  $l = 1, \dots, L$ .  $\kappa_{k,n}^{(l)}$  denotes the random phase shift of the  $l$ -th path. On the other hand, for sensing, apart from the sensing signals reflected from the target of interest, there also exists clutter interference which refers to the echo signals reflected by other objects. We assume the sampled signals returned by the clutter sources have a similar form as the reflected sensing signal in (9) and are given by [6]

$$\mathbf{c}_{k,n} = G \sum_{c=1}^C e^{j\omega_{k,n}^{(c)}} \xi_{k,n}^{(c)} \beta_{k,n}^{(c)} \mathbf{b}(\psi_{k,n}^{(c)}, \chi_{k,n}^{(c)}) \times \mathbf{a}^H(\psi_{k,n}^{(c)}, \chi_{k,n}^{(c)}) \mathbf{f}_{k,n}, \quad (36)$$

where  $C$  is the number of clutter sources. We note that the clutter sources are in general different from the scatterers in the communication channel.  $\omega_{k,n}^{(c)}$  denotes a random phase shift of the  $c$ -th path, and  $\beta_{k,n}^{(c)}$  is the path loss defined similarly as  $\beta_{k,n}$  in (6). We consider the radar cross-sections of the clutter sources are identical to that of the target vehicle and the path loss exponent in  $\beta_{k,n}^{(c)}$  is set to 4.8.  $\psi_{k,n}^{(c)}$  and  $\chi_{k,n}^{(c)}$  are the azimuth and elevation AoAs of the  $c$ -th clutter source, respectively. Furthermore, we assume  $\xi_{k,n}^{(c)} = \xi_{k,n}$ , for  $c = 1, \dots, C$ . At the RSU, the clutter interference is treated as noise, and the power of the clutter interference is given by  $\|\mathbf{c}_{k,n}\|^2$ . As a result, the total noise power impairing to the received sensing signal (9) is equal to  $\|\mathbf{c}_{k,n}\|^2 + \sigma_r^2$ . In Fig. 15, we present the achievable sum-rate for the multipath scenario. We assume the number of clutter sources to be 0, 5, and 20, respectively. We present the achievable sum-rate versus the number of non-LoS paths,  $L$ . The results demonstrate that the achievable sum-rate increases with the number of non-LoS paths. This is due to the fact that the additional non-LoS components further enhance the energy of the channel and lead to an improved received signal power at the

that ground reflections with AoDs and AoAs independent from those of the LoS channel can introduce additional interference and affect the system performance. We leave the investigation of the impact of such ground reflections for future work.



vehicles. While the reflected sensing signals do not contain the angular information of the non-LoS components, the DNNs can capture the spatial correlation between the LoS link and non-LoS components via offline training when given the reflected sensing signals as input and the overall communication channel in (35) as the label. In particular, the DNNs can extract the information of the LoS link based on the reflected sensing signals, and then map this information with the overall communication channel (including the non-LoS components). Thus, when performing online beamforming prediction, the proposed DNNs can infer the spatial correlations between LoS and non-LoS components based on the reflected sensing signals. Furthermore, there is only a 6% performance degradation of the proposed OSPB and TSPB schemes when the number of clutter sources increases from 0 to 20. This demonstrates the robustness of the proposed schemes against clutter. This is because the DNNs possess the ability to tackle such uncertainties.

### F. Signaling Overhead Analysis

In this subsection, we evaluate the signaling overhead required for both proposed schemes. For the OSPB scheme, the signaling overhead is due to the transmission of the predicted receive beamformers from the RSU to the corresponding vehicles. Each receive beamformer is a complex-valued vector of size  $M$ . Thus, the signaling overhead incurred by sending the receive beamformer increases linearly with respect to  $M$ . To reduce the signaling overhead, various beamformer quantization approaches can be employed. As an example, when considering a beam steering codebook for the receive beamformer quantization, the codebook has the same form of the array response vector  $\mathbf{u}(\varphi, \vartheta)$ , which is parameterized by the azimuth and elevation angles. Since the altitude of the RSU and the position of the road are fixed, the elevation angle  $\vartheta$  between the RSU and vehicles remains constant and is available at the RSU. We define a codebook  $\mathcal{W}$  which is quantized by  $N_q$  bits. The codebook consists of beam steering vectors  $\mathbf{u}(\frac{\pi q}{2N_q}, \vartheta)$ , where the variable  $q$  takes the values  $0, \dots, 2^{N_q} - 1$ . Given the receive beamformers obtained by the OSPB scheme, i.e.,  $\mathbf{w}_{k,n}$ , for the  $k$ -th vehicle and  $n$ -th time slot, the RSU selects the quantized beamformer  $\hat{\mathbf{w}}_{k,n}^q$  from the codebook based on the following optimization problem:

$$\hat{\mathbf{w}}_{k,n}^q = \arg \max_{\mathbf{w}_{k,n}^q \in \mathcal{W}} \left| \mathbf{w}_{k,n}^H \mathbf{w}_{k,n}^q \right|. \quad (37)$$

Then, the RSU sends the index of the selected beamformer to each vehicle and the signaling overhead can be reduced to  $N_q$  bits. In Fig. 16, we evaluate the impact of the codebook resolution  $N_q$  on the achievable sum-rate. We show the performance of the OSPB scheme with and without receive beamformer quantization, denoted by “OSPB (w/ quantization)” and “OSPB (w/o quantization)”, respectively. The total number of antennas at the vehicle  $M$  is set to 64. Two UPA architectures (i.e.,  $16 \times 4$  and  $8 \times 8$ ) at the vehicle are considered. The results in Fig. 16 reveal that using a  $16 \times 4$  UPA at the vehicle outperforms the  $8 \times 8$  UPA. This is because a larger number of horizontal antennas introduces more DoFs in the horizontal domain which

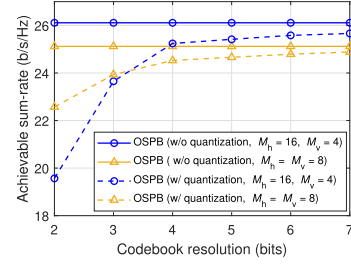


Fig. 16. Achievable sum-rate of the OSPB scheme with and without receive beamformer quantization ( $P = 30$  dBm,  $K = 4$ ,  $N_t = N_r = 256$ ).

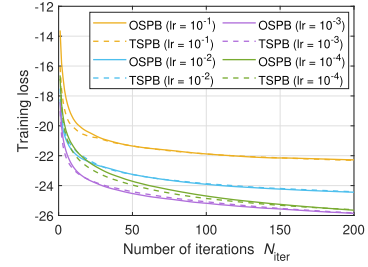


Fig. 17. Convergence performance of the proposed schemes ( $P = 30$  dBm,  $K = 4$ ,  $N_t = N_r = 256$ ,  $M = 64$ ).

is beneficial for interference management, thereby resulting in a higher achievable sum-rate. For both UPA architectures, it can be observed from the figure that a 3-bit codebook is sufficient to achieve 90% of the performance of the OSPB scheme without quantization.

For the TSPB scheme, instead of transmitting the predicted receive beamformers from the RSU to the vehicles at the end of each time slot, the vehicles download the predictive model from the RSU once the communication links have been established. The corresponding signaling overhead is determined by the number of parameters of the predictive model. For the DNN in the TSPB scheme, we use two FC layers at the vehicle for receive beamformer prediction, where the DNN outputs the real and imaginary parts of the beamformer separately. The number of parameters increases linearly with the number of antennas at each vehicle,  $M$ . When  $M$  is equal to 32, the total number of parameters is equal to 32,768. Considering typical Python-based implementations, each parameter of the DNN is a 32-bit real number. Thus, the total size of the DNN parameters at the vehicle side is equal to 1.048 Mbits. Moreover, various approaches, such as model compression techniques [36], have been proposed in the literature to facilitate DNN model download through downlink wireless channels. As this is not the main focus of our work, we do not provide a detailed discussion of this aspect. However, we note that for the proposed TSPB scheme, during data transmission, the RSU does not need to send the beamformer to the vehicles, and thus no additional signaling overhead is incurred.

### G. Convergence Performance

Next, we show the convergence performance of the proposed schemes in Fig. 17. We evaluate the learning rates (denoted as

TABLE I  
ONLINE EXECUTION RUNTIME COMPARISON

Setting	EKF	OSPB	TSPB	
			RSU	Vehicle
$N_t = N_r = 64$ $M = 64, K = 4$	25 ms	1.18 ms	1.14 ms	0.031 ms
$N_t = N_r = 256$ $M = 64, K = 4$	309 ms	1.77 ms	1.73 ms	0.032 ms
$N_t = N_r = 256$ $M = 100, K = 4$	309 ms	1.79 ms	1.74 ms	0.034 ms
$N_t = N_r = 256$ $M = 100, K = 8$	617 ms	3.31 ms	3.27 ms	0.034 ms

“lr” in Fig. 17) on the convergence performance. The results indicate that the use of a large learning rate (e.g.,  $10^{-1}$  or  $10^{-2}$ ) can facilitate rapid convergence of the DNNs, but it may not necessarily lead to convergence to a desirable trained result. On the other hand, a smaller learning rate (e.g.,  $10^{-4}$ ) requires more training epochs to converge. In our work, when the learning rate is set to be  $10^{-3}$ , the DNNs can converge to a satisfactory result within 100 training epochs.

#### H. Runtime Comparison

Finally, in Table I, we evaluate the online execution runtime for the proposed schemes. We conducted our simulations using a computing server with an Intel Core i7-10700 @ 3.80GHz CPU and an NVIDIA GeForce RTX 3070 GPU. We compare the online runtime of our proposed OSPB and TSPB schemes with that of the EKF scheme in [12]. The batch size is set to 10 for the OSPB and TSPB schemes. For the proposed TSPB scheme, we include the computational time for the RSU and each vehicle. The results show that the proposed schemes are more efficient than the EKF scheme in terms of the runtime. The RSU can predict the transmit beamformer within a few milliseconds. On the vehicle side, the predictive model is computationally efficient, placing minimal computation burden on the vehicles.

## VI. CONCLUSION

In this paper, we investigated the ISAC-enabled end-to-end predictive beamforming design in V2I networks. The proposed OSPB and TSPB schemes predict the beamformers directly from the reflected sensing signals via DNNs which bypass the state parameter estimation phase. Both schemes jointly determine the transmit and receive beamformers. Our simulation results demonstrated the advantages of the end-to-end design and the effectiveness of the developed DNNs of the proposed schemes compared to existing approaches. Furthermore, due to the joint design of the transmit and receive beamformers, the proposed schemes can effectively manage inter-user interference. Our simulation results also revealed that the proposed schemes are robust to the impairment of the reflected sensing signals due to clutter. For future work, it is of interest to consider a more general system model, where vehicles move along arbitrarily shaped roads. Furthermore, since mmWave channels are sensitive to blockages, blockage prediction and avoidance are worth

studying for V2I networks. Simulating the wireless channels using ray tracing techniques is also of interest for analyzing the performance of the developed predictive beamforming schemes.

## REFERENCES

- [1] Z. Wang and V. W.S. Wong, “Deep learning for ISAC-enabled end-to-end predictive beamforming in vehicular networks,” in *Proc. IEEE Int. Conf. Commun.*, Rome, Italy, May 2023, pp. 5713–5718.
- [2] Z. Zhang et al., “6G wireless networks: Vision, requirements, architecture, and key technologies,” *IEEE Veh. Technol. Mag.*, vol. 14, no. 3, pp. 28–41, Sep. 2019.
- [3] H. Tataria, M. Shafi, A. F. Molisch, M. Dohler, H. Sjöland, and F. Tufveson, “6G wireless systems: Vision, requirements, challenges, insights, and opportunities,” *Proc. IEEE*, vol. 109, no. 7, pp. 1166–1199, Jul. 2021.
- [4] J. A. Zhang et al., “An overview of signal processing techniques for joint communication and radar sensing,” *IEEE J. Sel. Topics Signal Process.*, vol. 15, no. 6, pp. 1295–1315, Nov. 2021.
- [5] K. B. Letaief, W. Chen, Y. Shi, J. Zhang, and Y.-J. A. Zhang, “The roadmap to 6G: AI empowered wireless networks,” *IEEE Commun. Mag.*, vol. 57, no. 8, pp. 84–90, Aug. 2019.
- [6] F. Liu et al., “Integrated sensing and communications: Toward dual-functional wireless networks for 6G and beyond,” *IEEE J. Sel. Areas Commun.*, vol. 40, no. 6, pp. 1728–1767, Jun. 2022.
- [7] A. Liu et al., “A survey on fundamental limits of integrated sensing and communication,” *IEEE Commun. Surveys Tuts.*, vol. 24, no. 2, pp. 994–1034, Second Quarter 2022.
- [8] F. Liu, L. Zhou, C. Masouros, A. Li, W. Luo, and A. Petropulu, “Toward dual-functional radar-communication systems: Optimal waveform design,” *IEEE Trans. Signal Process.*, vol. 66, no. 16, pp. 4264–4279, Aug. 2018.
- [9] F. Liu, C. Masouros, A. Li, H. Sun, and L. Hanzo, “MU-MIMO communications with MIMO radar: From co-existence to joint transmission,” *IEEE Trans. Wireless Commun.*, vol. 17, no. 4, pp. 2755–2770, Apr. 2018.
- [10] X. Liu, T. Huang, N. Shlezinger, Y. Liu, J. Zhou, and Y. C. Eldar, “Joint transmit beamforming for multiuser MIMO communications and MIMO radar,” *IEEE Trans. Signal Process.*, vol. 68, pp. 3929–3944, 2020.
- [11] C. G. Tsinos, A. Arora, S. Chatzinotas, and B. Ottersten, “Joint transmit waveform and receive filter design for dual-function radar-communication systems,” *IEEE J. Sel. Topics Signal Process.*, vol. 15, no. 6, pp. 1378–1392, Nov. 2021.
- [12] F. Liu, W. Yuan, C. Masouros, and J. Yuan, “Radar-assisted predictive beamforming for vehicular links: Communication served by sensing,” *IEEE Trans. Wireless Commun.*, vol. 19, no. 11, pp. 7704–7719, Nov. 2020.
- [13] W. Yuan, F. Liu, C. Masouros, J. Yuan, D. W. K. Ng, and N. González-Prelcic, “Bayesian predictive beamforming for vehicular networks: A low-overhead joint radar-communication approach,” *IEEE Trans. Wireless Commun.*, vol. 20, no. 3, pp. 1442–1456, Mar. 2021.
- [14] J. Mu, Y. Gong, F. Zhang, Y. Cui, F. Zheng, and X. Jing, “Integrated sensing and communication-enabled predictive beamforming with deep learning in vehicular networks,” *IEEE Commun. Lett.*, vol. 25, no. 10, pp. 3301–3304, Oct. 2021.
- [15] C. Liu et al., “Learning-based predictive beamforming for integrated sensing and communication in vehicular networks,” *IEEE J. Sel. Areas Commun.*, vol. 40, no. 8, pp. 2317–2334, Aug. 2022.
- [16] J. A. Zhang, X. Huang, Y. J. Guo, J. Yuan, and R. W. Heath Jr., “Multi-beam for joint communication and radar sensing using steerable analog antenna arrays,” *IEEE Trans. Veh. Technol.*, vol. 68, no. 1, pp. 671–685, Jan. 2019.
- [17] P. Kumari, S. A. Vorobyov, and R. W. Heath Jr., “Adaptive virtual waveform design for millimeter-wave joint communication-radar,” *IEEE Trans. Signal Process.*, vol. 68, pp. 715–730, 2020.
- [18] J. Liu, K. V. Mishra, and M. Saquib, “Transceiver co-design for full-duplex integrated sensing and communications,” in *Proc. IEEE Glob. Commun. Conf.*, Rio de Janeiro, Brazil, Dec. 2022, pp. 3821–3826.
- [19] T. Wei, L. Wu, K. V. Mishra, and M. R. B. Shankar, “Simultaneous active-passive beamforming design in IRS-enabled multi-carrier DFRC system,” in *Proc. IEEE Eur. Signal Process. Conf.*, Belgrade, Serbia, Aug. 2022, pp. 1007–1011.
- [20] M. Noor-A-Rahim et al., “6G for vehicle-to-everything (V2X) communications: Enabling technologies, challenges, and opportunities,” *Proc. IEEE*, vol. 110, no. 6, pp. 712–734, Jun. 2022.

- [21] A. M. Elbir, K. V. Mishra, and S. Chatzinotas, "Terahertz-band joint ultra-massive MIMO radar-communications: Model-based and model free hybrid beamforming," *IEEE J. Sel. Topics Signal Process.*, vol. 15, no. 6, pp. 1468–1483, Nov. 2021.
- [22] S. H. Dokhanchi, M. R. B. Shankar, M. Alaei-Kerahroodi, and B. Ottersten, "Adaptive waveform design for automotive joint radar-communication systems," *IEEE Trans. Veh. Techn.*, vol. 70, no. 5, pp. 4273–4290, May 2021.
- [23] P. Kumari, N. J. Mayers, and R. W. Heath Jr., "Adaptive and fast combined waveform-beamforming design for mmWave automotive joint communication-radar," *IEEE J. Sel. Topics Signal Process.*, vol. 15, no. 4, pp. 996–1012, Jun. 2021.
- [24] F. Liu and C. Masouros, "A tutorial on joint radar and communication transmission for vehicular networks—Part III: Predictive beamforming without state models," *IEEE Commun. Lett.*, vol. 25, no. 2, pp. 332–336, Feb. 2021.
- [25] W. Yuan, Z. Wei, S. Li, J. Yuan, and D. W. K. Ng, "Integrated sensing and communication-assisted orthogonal time frequency space transmission for vehicular networks," *IEEE J. Sel. Topics Signal Process.*, vol. 15, no. 6, pp. 1515–1528, Nov. 2021.
- [26] C. B. Barneto, S. D. Liyanaarachchi, M. Henino, T. Riihonen, and M. Valkama, "Full duplex radio/radar technology: the enabler for advanced joint communication and sensing," *IEEE Wireless Commun.*, vol. 28, no. 1, pp. 82–88, Feb. 2021.
- [27] R. W. Heath Jr and A. Lozano, *Foundations of MIMO Communication*. Cambridge, U.K.: Cambridge Univ. Press, 2018.
- [28] K. M. Attiah, F. Sohrabi, and W. Yu, "Deep learning for channel sensing and hybrid precoding in TDD massive MIMO OFDM systems," *IEEE Trans. Wireless Commun.*, vol. 21, no. 12, pp. 10839–10853, Dec. 2022.
- [29] A.-A. Lu, X. Gao, X. Meng, and X.-G. Xia, "Omnidirectional precoding for 3D massive MIMO with uniform planar arrays," *IEEE Trans. Wireless Commun.*, vol. 19, no. 4, pp. 2628–2642, Apr. 2020.
- [30] M. A. Richards, *Fundamentals of Radar Signal Processing*, 3rd ed. New York, NY, USA: McGraw Hill, 2022.
- [31] E. Björnson, J. Hoydis, and L. Santuini, "Massive MIMO networks: Spectral, energy, and hardware efficiency," *Found. Trends Signal Process.*, vol. 11, no. 3/4, pp. 154–655, 2017.
- [32] G. Hakobyan and B. Yang, "High-performance automotive radar: A review of signal processing algorithms and modulation schemes," *IEEE Signal Process. Mag.*, vol. 36, no. 5, pp. 32–44, Sep. 2019.
- [33] Y. Niu, Y. Li, D. Jin, L. Su, and A. V. Vasilakos, "A survey of millimeter wave (mmWave) communications for 5G: Opportunities and challenges," *Wireless Netw.*, vol. 21, no. 8, pp. 2657–2676, Nov. 2015.
- [34] D. Bahdanau, K. Cho, and Y. Bengio, "Neural machine translation by jointly learning to align and translate," in *Proc. Int. Conf. Learn. Representations*, San Diego, CA, May 2015.
- [35] D. P. Kingma and J. L. Ba, "Adam: A method for stochastic optimization," in *Proc. Int. Conf. Learn. Representations*, San Diego, CA, May 2015.
- [36] Y. Choi, M. El-Khamy, and J. Lee, "Universal deep neural network compression," *IEEE J. Sel. Topics Signal Process.*, vol. 14, no. 4, pp. 715–726, May 2020.



**Zihuan Wang** (Student Member, IEEE) received the B.S. and M.S. degrees from the Dalian University of Technology, Dalian, China, in 2017 and 2020, respectively. She is currently working toward the Ph.D. degree with the Department of Electrical and Computer Engineering, The University of British Columbia (UBC), Vancouver, BC, Canada. Her research interests include machine learning and optimization for wireless networks, with a main focus on integrated sensing and communication systems and millimeter-wave MIMO systems. She is also an Assistant to Editor-in-Chief of IEEE TRANSACTIONS ON WIRELESS COMMUNICATIONS. She was the recipient of UBC's Four Year Fellowship (2020–2024), Li Tze Fong Memorial Fellowship (2023–2024), Graduate Support Initiative Award (2021–2023) from the Faculty of Applied Science at UBC, and Best Paper Award at the IEEE ICC 2022.



**Vincent W.S. Wong** (Fellow, IEEE) received the B.Sc. degree from the University of Manitoba, Winnipeg, MB, Canada, in 1994, the M.A.Sc. degree from the University of Waterloo, Waterloo, ON, Canada, in 1996, and the Ph.D. degree from the University of British Columbia (UBC), Vancouver, BC, Canada, in 2000. From 2000 to 2001, he was a Systems Engineer with PMC-Sierra Inc. (now Microchip Technology Inc.). In 2002, he joined the Department of Electrical and Computer Engineering, UBC, and is currently a Professor. His research includes protocol design, optimization, and resource management of communication networks, with applications to 5G/6G wireless networks, Internet of things, mobile edge computing, smart grid, and energy systems. Dr. Wong is also the Editor-in-Chief of IEEE TRANSACTIONS ON WIRELESS COMMUNICATIONS. He was an Area Editor of IEEE TRANSACTIONS ON COMMUNICATIONS and IEEE OPEN JOURNAL OF THE COMMUNICATIONS SOCIETY, an Associate Editor for IEEE TRANSACTIONS ON MOBILE COMPUTING and IEEE TRANSACTIONS ON VEHICULAR TECHNOLOGY, and a Guest Editor of IEEE JOURNAL ON SELECTED AREAS IN COMMUNICATIONS, IEEE INTERNET OF THINGS JOURNAL, and IEEE WIRELESS COMMUNICATIONS. From 2019 to 2020, he was an IEEE Communications Society Distinguished Lecturer and is also an IEEE Vehicular Technology Society Distinguished Lecturer for the term of 2023–2025. He was the General Co-Chair of IEEE INFOCOM 2024, Tutorial Co-Chair of IEEE GLOBECOM 2018, Technical Program Co-Chair of IEEE VTC2020 -Fall and IEEE SmartGridComm 2014, and Symposium Co-Chair of IEEE ICC'18, IEEE SmartGridComm ('13, '17) and IEEE GLOBECOM'13. He was the recipient of the 2022 Best Paper Award from IEEE Transactions on Mobile Computing and Best Paper Awards at the IEEE ICC 2022 and IEEE GLOBECOM 2020. He was also the Chair of the IEEE Vancouver Joint Communications Chapter and IEEE Communications Society Emerging Technical Sub-Committee on Smart Grid Communications. He is a Fellow of the Engineering Institute of Canada (EIC).



**Robert Schober** (Fellow, IEEE) received the Diploma (Univ.) and the Ph.D. degree in electrical engineering from the Friedrich-Alexander University of Erlangen-Nuremberg (FAU), Erlangen, Germany, in 1997 and 2000, respectively. From 2002 to 2011, he was a Professor and Canada Research Chair with the University of British Columbia (UBC), Vancouver, BC, Canada. Since January 2012, he has been an Alexander von Humboldt Professor and the Chair for Digital Communication with FAU. Since 2017, he has been listed as a Highly Cited Researcher by the Web of Science. His research interests include the broad areas of communication theory, wireless and molecular communications, and statistical signal processing. He was the recipient of the several awards for his work including the 2002 Heinz Maier Leibnitz Award of the German Science Foundation (DFG), 2004 Innovations Award of the Vodafone Foundation for Research in Mobile Communications, 2006 UBC Killam Research Prize, 2007 Wilhelm Friedrich Bessel Research Award of the Alexander von Humboldt Foundation, 2008 Charles McDowell Award for Excellence in Research from UBC, 2011 Alexander von Humboldt Professorship, 2012 NSERC E.W.R. Stacie Fellowship, 2017 Wireless Communications Recognition Award by the IEEE Wireless Communications Technical Committee, and 2022 IEEE Vehicular Technology Society Stuart F. Meyer Memorial Award, and numerous Best Paper awards for his work including the 2022 ComSoc Stephen O. Rice Prize and the 2023 ComSoc Leonard G. Abraham Prize. He was Editor-in-Chief of IEEE TRANSACTIONS ON COMMUNICATIONS, VP Publications of the IEEE Communication Society (ComSoc), ComSoc Member at Large, and ComSoc Treasurer. He is also the Senior Editor of the Proceedings of the IEEE and as ComSoc President. He is also a Fellow of the Canadian Academy of Engineering and Engineering Institute of Canada, and the Member of the German National Academy of Science and Engineering.